

PORE-LEVEL ENGINEERING OF MICROSTRUCTURED FUNCTIONAL MEDIA
WITH APPLICATIONS TO THERMAL PROPERTIES

By

ANUPAM AKOLKAR

A THESIS PRESENTED TO THE GRADUATE SCHOOL
OF THE UNIVERSITY OF FLORIDA IN PARTIAL FULFILLMENT
OF THE REQUIREMENTS FOR THE DEGREE OF
MASTER OF SCIENCE

UNIVERSITY OF FLORIDA

2012

© 2012 Anupam Akolkar

To
All good men (and women) who came to the aid of the party

ACKNOWLEDGMENTS

Acknowledgments are due to Dr. Petrasch, my committee chairman, whose unwavering faith in me, coupled with his impeccable knowledge subject-matter, made this level of research possible within a short time. I would like to thank Drs. Hahn and Klausner for contributing not only to the technical aspects of this study but also to my general well-being and focus. I would like to thank my lab-mates Abhishek Singh, Midori Takagi and Benjamin Erickson for aiding me and encouraging me throughout the time spent at the Energy Research and Education Park.

Lastly, I would like to thank my parents, my brother and my extended family for the support they have given me over the duration of my education, my friends for constantly reminding me that I am capable of exceeding my earlier achievements and my fellow students who chipped in with suggestions and solutions whenever approached.

TABLE OF CONTENTS

	<u>page</u>
ACKNOWLEDGMENTS	4
LIST OF TABLES	7
LIST OF FIGURES	8
LIST OF ABBREVIATIONS.....	10
LIST OF SYMBOLS	11
ABSTRACT.....	15
CHAPTER	
1 POROUS MEDIA – FUNDAMENTALS AND APPLICATIONS	17
1.1 Porous Media.....	17
1.2 Tomography Data and Pore-Level Geometry.....	18
1.2.1 Tomographic Reconstruction of Porous Medium Datasets.....	18
1.2.2 Manipulating Tomography Datasets	21
1.2.2.1 Removing noise and meso-porosity	21
1.2.2.2 Erosions and dilations to simulate porosity variation	21
1.3 Summary.....	25
2 RADIATIVE HEAT TRANSFER	27
2.1 Radiative Transfer in Porous Media	27
2.2 Methodology.....	28
2.2.1 The Monte Carlo Method	29
2.2.2 Analytical Model	32
2.2.3 Convergence Study.....	34
2.3 Results.....	35
2.4 Summary	41
3 FLUID FLOW	43
3.1 Fluid Flow in Porous Media	43
3.2 Theory.....	44
3.2.1 Darcy’s Law, Permeability and Dupuit-Forchheimer Coefficient	44
3.2.2 Analytical Flow Models	46
3.2.2.1 Models for permeability	46
3.2.2.2 Models for Dupuit-Forchheimer coefficient (non-Darcy coefficient):	50
3.3 Methodology.....	51
3.3.1 Mesh Generation and Flow Simulation.....	52

3.3.2 Representative Mesh and Sample Length Scales	55
3.4 Results.....	58
3.5 Summary.....	64
4 SCOPE AND OUTLOOK.....	66
4.1 Accomplishments	66
4.2 Future Scope	66
4.2.1 Solid Phase Conduction and Combined Conduction, Convection and Radiation Modeling	66
4.2.2 Multi-objective Optimization and Transient Process Simulation	67
4.3 Tailored Media.....	67
LIST OF REFERENCES	68
BIOGRAPHICAL SKETCH	74

LIST OF TABLES

<u>Table</u>		<u>page</u>
1-1	Tomography data for model media.....	20
2-1	Extinction correlation coefficient, c, forward scattering fraction, k, and asymmetry factor, g, for the media studied	37
3-1	Porosities and specific surface areas of the samples employed.....	52
3-2	Permeability and Dupuit-Forchheimer coefficient values for the RPC and CaCO ₃ packed bed samples as identified from direct pore level simulation.	58
3-3	RMS errors of the results for permeability for different models, across all porosities, for the sample media.	60
3-4	RMS errors of the results for predicted Dupuit-Forchheimer coefficient, across all porosities, for the sample media	62

LIST OF FIGURES

<u>Figure</u>	<u>page</u>
1-1	Representative Elementary Volume calculations of original samples for a) RPC, $\epsilon = 0.913$ and b) CaCO_3 , $\epsilon = 0.604$20
1-2	2-point correlation functions of original samples for a) RPC, $\epsilon = 0.913$ and b) CaCO_3 , $\epsilon = 0.604$21
1-3	Morphological operations performed on RPC: (a) segmented sample image obtained from original tomography data, (b) image after iterative openings and closings to remove meso-scale porosity, (c) after addition of a layer 144 μm thick (d) after removal of a layer 120 μm thick.23
1-4	Morphological operations performed on tomography data for the packed CaCO_3 particle bed: (a) original data, (b) after segmentation and openings to remove noise (c) after addition of a layer 225 μm thick, (d) after removal of a layer 180 μm thick.24
1-5	Specific surface area vs. porosity for a) RPC and b) CaCO_3 samples.25
2-1	Simulated system and boundary conditions.31
2-2	Surface reflections in RPC sample of $\epsilon = 0.913$ at $\rho = 0.65$, with specular surfaces. Notice the penetration of radiation in the irradiated direction (+X). Even at high porosity, the transmission through the sample is low.31
2-3	MC convergence study for an RPC sample of porosity $\epsilon = 0.8351$ and a CaCO_3 packed particle bed sample of porosity $\epsilon = 0.4577$ for diffuse surfaces, irradiated with diffuse radiation.35
2-4	Transmittance and reflectance for diffusely irradiated RPC sample, in case of (a) diffuse solid phase (b) specular solid phase. Here, $\epsilon_1 = 0.727$, $\epsilon_2 = 0.863$, $\epsilon_3 = 0.964$36
2-5	Transmittance and reflectance for RPC sample irradiated with collimated radiation, in case of (a) diffuse solid phase (b) specular solid phase. Here, $\epsilon_1 = 0.727$, $\epsilon_2 = 0.863$, $\epsilon_3 = 0.964$38
2-6	Transmittance and reflectance for CaCO_3 particle packed bed sample irradiated with diffuse radiation, in case of (a) diffuse solid phase (b) specular solid phase. Here, $\epsilon_1 = 0.159$, $\epsilon_2 = 0.604$, $\epsilon_3 = 0.904$38
2-7	Transmittance and reflectance of CaCO_3 particle packed bed for sample irradiated with collimated radiation, in case of (a) diffuse solid phase (b) specular solid phase. Here, $\epsilon_1 = 0.159$, $\epsilon_2 = 0.604$, $\epsilon_3 = 0.904$40

2-8	Absorptance RPC (a) and CaCO ₃ particle packed bed (b), for diffuse radiation and diffuse solid phases, with solid phase $\rho = 0.65$. The dotted line indicates the local optimal porosity as a function of L/d_{nom}	40
3-1	Computational domain and boundary conditions.	53
3-2	Sectional views of tetrahedral grids generated in pore-space of (a) RPC sample R1 and (b) CaCO ₃ particle bed sample C3. It can be seen that the grid is very fine and dense at the solid-void interface and element sizes rapidly converge to the preset maximum.	54
3-3	Dimensionless pressure along the length of a sample for increasing Reynolds numbers: (a) RPC sample R3 and (b) CaCO ₃ particle packed bed sample C3. For Re 0.1-1.0, the profiles overlap as the pressure drop is governed by permeability alone, at higher Re, the Dupuit-Forchheimer term starts to become distinct, and dimensionless pressure drop increases.....	54
3-4	Pressure drop convergence vs. grid refinement for (a) RPC sample R1 and (b) CaCO ₃ particle packed bed sample C3.	56
3-5	Convergence of pressure drop per unit length vs. sample size for (a) RPC sample R1 and (b) CaCO ₃ particle packed bed sample C3.....	57
3-6	DPLS results and fitting results for normalized pressure drops for (a) RPC samples and (b) CaCO ₃ packed bed samples.....	59
3-7	Permeability vs. porosity for (a) RPC samples and (b) CaCO ₃ packed bed samples.	59
3-8	Permeability vs. porosity for (a) RPC and (b) CaCO ₃ packed bed for corrected Kozeny constants. Also plotted are the DPLS results.....	61
3-9	Dupuit-Forchheimer coefficient vs. porosity for (a) RPC samples and (b) CaCO ₃ samples.....	62

LIST OF ABBREVIATIONS

CFD	Computational Fluid Dynamics
DPLS	Direct, pore-level numerical simulation
MCRT	Monte Carlo Ray Tracing
NRMSE	Normalized RMS Error
REV	Representative Elementary Volume
RMSE	Root Mean Square Error
RPC	Reticulated porous ceramic
RTE	Radiative Transfer Equation

LIST OF SYMBOLS

Alphabetical symbols

a	Particle size distribution constant (-)
A	overall absorptance of medium sample (-)
A_0	Specific surface area (m ⁻¹)
b	Constant in Cooke's Dupuit-Forchheimer coefficient correlation (-)
c	correlation constant for extinction coefficient (-)
c_0	Inverse dimensionless permeability (-)
c_1	Dimensionless Dupuit-Forchheimer coefficient (-)
C_Δ	Relative convergence of pressure drop with mesh refinement (-)
C_V	Relative convergence of pressure drop with sample size (-)
d	Diameter (hydraulic) (m)
d_f	Fiber diameter (m)
d_{nom}	nominal diameter (m)
d_p	Particle diameter (m)
d_{solid}	Solid phase hydraulic diameter (m)
d_{void}	Void phase hydraulic diameter (m)
f_d	Friction factor due to fiber deflection (-)
F	Dupuit-Forchheimer coefficient (m ⁻¹)
g	asymmetry factor (-)
I^+	intensity in the forward direction along normal to irradiated plane (-)
I^-	intensity in the backward direction along normal to irradiated plane (-)
k	forward scattering fraction (-)
k_4, k_5	Constants in Davies' equation (-)
k_K	Kozeny constant (-)

K	permeability (m ²)
L	Sample length (m)
L_{REV}	edge length of Representative Elementary Volume (REV) (m)
m	Constant in Cooke's Dupuit-Forchheimer coefficient correlation (-)
n	generic constant in relations for Dupuit-Forchheimer coefficient correlation (-)
$\hat{\mathbf{n}}$	surface normal
N_e	Effective pore number (-)
N_{rays}	number of stochastic rays irradiating the volume
N_x, N_y, N_z	number of voxels in x-, y- and z- directions
P	Pressure (Pa)
P_0	starting point of a ray in fluid phase
P_i	point of incidence of a ray on the solid-void interface
q	constants of integration
r	Radial distance in sample volume (m)
R	overall reflectance of medium sample (-)
Re	Reynolds number (-)
s	distance travelled by ray in direction $\hat{\mathbf{s}}$ (m)
s_2	2-point correlation function (-)
$\hat{\mathbf{s}}$	initial direction of travel of a ray
T	overall transmittance of medium sample (-)
\mathbf{u}_D	Darcean velocity vector (ms ⁻¹)
u_D	Darcean velocity (ms ⁻¹)
V	Sample volume (m ³)
\mathbf{V}	eigenvectors

z Distance along sample axis (m)

Greek Symbols

α absorptivity (-)

β extinction coefficient of the medium (m⁻¹)

γ eigenvalues

δ Dirac Delta (-)

Δ voxel edge length (m)

ε medium porosity (-)

θ_i angle of incidence (rad)

θ_s scattering angle (rad)

λ wavelength of incoming radiation (m)

μ cosine of scattering angle (-)

μ Dynamic viscosity (Pa-s)

ξ size parameter (-)

ρ hemispherical reflectivity (-)

ρ' directional hemispherical reflectivity (-)

σ standard deviation for 3-D Gaussian filtering (m)

σ_s isotropic scattering coefficient (-)

ψ_0 interface gray value

$\psi_{(\text{bin})ijk}$ segmented binary dataset for porous material space

ψ_{ijk} gray value dataset obtained from tomography data

$\Psi(x)$ continuous, 3-D gray value function

φ azimuthal angle (rad)

Φ scattering phase function (-)

Ω solid angle (sr)

Subscripts

Br	Brinkman drag model
Ch	Chen fibrous bed model
CK	Carman-Kozeny model
Cond	Conduit flow model
Dav	Davies fibrous bed model
DPLS	Direct Pore Level Simulation
E	Ergun correlation for Dupuit-Forchheimer coefficient
G	Geertsma correlation
HB	Happel-Brenner parallel flow model
k	Kernel
Ky	Kyan fibrous bed model
M	Modified Ergun (Macdonald et al) correlation
s2a	2-point correlation approximation
W	Ward correlation
$\Delta\epsilon$	porosity variation band
Δ	voxel edge
rel	relative value
10^8	value calculated for 10^8 rays

Abstract of Thesis Presented to the Graduate School
of the University of Florida in Partial Fulfillment of the
Requirements for the Master of Science

PORE-LEVEL ENGINEERING OF MICROSTRUCTURED FUNCTIONAL MEDIA
WITH APPLICATIONS TO THERMAL PROPERTIES

By

Anupam Akolkar

May 2012

Chair: Jörg Petrasch
Cochair: David Hahn
Major: Aerospace Engineering

Tomography data of porous media is used to determine thermal properties of these media through direct, pore-level numerical simulation (DPLS) of radiative heat transfer and fluid flow. Two kinds of porous media have been studied: a) a 10 pores per inch (ppi) reticulated porous ceramic (RPC) and b) a packed bed of CaCO_3 particles. Digital image processing routines are applied to the tomography data to simulate porosity variation in the media and extend the results over a range of porosities in each case.

Radiative transfer in the media is studied for an opaque, diffuse or specular solid phase within a non-participating void phase and the results were applied to an analytical two-flux model to determine the extinction coefficient and forward-scattering fraction. Porosity for optimum absorption of incident radiation at a given sample thickness is determined. For the RPC, the forward scattering fraction varies between 0.38 and 0.57, and the extinction correlation coefficient varies between 9.56 and 7.03. For the packed CaCO_3 particle bed, the forward scattering fraction varies between 0.6 and 0.72, and the extinction coefficient varies between and 2.84 and 2.14.

Medium permeability and Dupuit-Forchheimer coefficients have been determined for selected samples of the media through fluid-flow simulations at Reynolds numbers varying from 0.1-200. The results have then been compared to existing flow models to determine their applicability to the media. An adjusted Kozeny constant has been determined for each medium. For the RPC, the Kozeny constant is evaluated at 7.73 and for the CaCO₃ packed bed, it is found to be 6.10, leading to predictions of the permeability with an NRMSE of 4.16% and 3.37% respectively.

CHAPTER 1
POROUS MEDIA – FUNDAMENTALS AND APPLICATIONS ^{*†}

1.1 Porous Media

Heat and mass transfer in porous media is of considerable interest in a variety of engineering applications [1,2]. These applications tend to utilize unique characteristics of transport through the pore-space in these media [3]. Modern applications of porous media include radiant burners [4,5], reactive media in hydrogen generation from naturally occurring hydrocarbons [6,7] and solar thermochemical production of hydrogen [8], catalytic converters for flue gases [9,10] and so on.

Design and optimization of applications using porous media often relies on continuum models of transport within these media [1]. These models use volume averaging [11] and effective transport properties of the media as determined through experimentation and analytical modeling. Experimental determination of properties is restricted to a casewise basis and endures errors and limits imposed by experimental conditions – overall a loss of generality occurs. It is also very difficult to analyze the effect of a particular topological parameter, say porosity, on a given transport property of the chosen porous medium, since close control on the properties of a manufactured specimen is very difficult [12]. Analytical models require simplification of the pore-level geometry through assumptions on the porous medium morphology and although they deliver wider applicability, they lack in accuracy [2].

^{*} Material from this chapter has been published in: A. Akolkar, J. Petrasch, Tomography based pore-level optimization of radiative transfer in porous media, *International Journal of Heat and Mass Transfer*. 54 (2011) 4775–4783.

[†] Material from this chapter has been submitted for publication in: A. Akolkar, J. Petrasch, Tomography Based Characterization and Optimization Of Fluid Flow Through Porous Media, *Transport in Porous Media*, submitted March 2012.

The application of high resolution tomography to acquire 3D geometry of porous media with a view to using this data in pore-level numerical simulation of transport phenomena in these media has been discussed in detail in [13]. This method allows for accurate representation of morphologies of media and also offers the possibility of studying the effect of variation of morphology, accomplished in this case through image-processing routines, on the transport characteristics of a given medium.

The present study employs this technique in parametric modeling of radiative heat transfer and fluid flow through two types of porous media: a) a 10 pores per inch (ppi) reticulated porous ceramic (RPC) a high-porosity artificial ceramic structure [3] and b) a packed bed of CaCO_3 particles. The media have been treated as macroporous [3] media with a rigid solid phase distributed in a connected void phase. Solid interconnectivity exists in the RPC whereas the CaCO_3 particle packed bed consists of randomly shaped, disconnected particles. The pore-level geometry of the media is incrementally modified using digital image processing routines of *erosion* and *dilation* [14], to simulate porosity variation in the samples.

1.2 Tomography Data and Pore-Level Geometry

1.2.1 Tomographic Reconstruction of Porous Medium Datasets

Tomography data used in [15,16] has been used in this thesis for the RPC and the CaCO_3 particle packed bed respectively. In each case the data has been obtained as a N_z 8-bit grayscale images of $N_x \times N_y$ pixels each, so that a 3D set of gray values ψ_{ijk} of $N_x \times N_y \times N_z$ voxels, each of edge length Δ is available. Collection of micron and submicron-scale tomography data has been discussed in [13]. Defining the porous medium as an intersection of two compact sets F (fluid or void phase) and S (solid phase) in \mathbb{R}^3 , the solid-void interface is defined as $I = F \cap S$. An interface gray value ψ_0 , is obtained using the method of modes [14]. Also defined is the binary gray-value dataset, $\psi_{(\text{bin})ijk}$, by segmenting the dataset:

$$\psi_{(\text{bin})ijk} = \begin{cases} 0 & \text{if } \psi_{ijk} < \psi_0 \\ 1 & \text{if } \psi_{ijk} \geq \psi_0 \end{cases} \quad (1-1)$$

From this, the porosity, defined as the fraction of the void-phase volume to the total medium volume, is calculated as:

$$\varepsilon = \frac{V(F)}{V(P)} = \frac{\sum_{k=1}^{N_z} \sum_{j=1}^{N_y} \sum_{i=1}^{N_x} \psi_{(\text{bin})ijk}}{N_x \times N_y \times N_z} \quad (1-2)$$

The gray-value dataset is smoothed using a Gaussian kernel with standard deviation σ_k and length Δ_k whereupon a smoothed gray-level function $\psi(\mathbf{r})$ is obtained. The two-point correlation function is defined as the probability that two arbitrary points in the porous medium separated by a distance r are both in the void (fluid) phase. This is calculated using a large number of realizations n as:

$$s_2(r) = \frac{\int \int \psi(\mathbf{r})\psi(\mathbf{r} + r\hat{\mathbf{s}})d\hat{\mathbf{s}}dr}{4\pi V(P)} \approx \frac{\sum_{i=1}^n \psi(\mathbf{r}_i)\psi(\mathbf{r}_i + r\hat{\mathbf{s}}_i)}{n} \quad (1-3)$$

Here, \mathbf{r}_i are randomly and uniformly distributed points in the medium space, $\hat{\mathbf{s}}_i$ are uniformly distributed direction vectors and the distance between the two points where ψ is checked, r , is also uniformly distributed [13]. The specific surface of the porous medium, defined as the interface area $A(I)$ per unit medium volume, is found using [17]:

$$\left. \frac{ds_2}{dr} \right|_{r=0} = -\frac{A_0}{4} \quad (1-4)$$

A subset of a porous medium that is large enough, so that the medium can be considered a continuum is called a Representative Elementary Volume (REV). The edge length of the smallest cuboidal subset of the medium sample beyond which the porosity of the medium stays

within a small band $\varepsilon \pm \Delta\varepsilon$ is denoted as $L_{\text{REV},\Delta\varepsilon}$. This value is calculated by statistical sampling over a large number of randomly originating sample cubes within the medium [17].

Relevant tomography data for the original datasets of the model media are given in table 1-1 below. Figures 1-1, 1-2 show sample plots for L_{REV} and the s_2 correlation for the original samples of the model media.

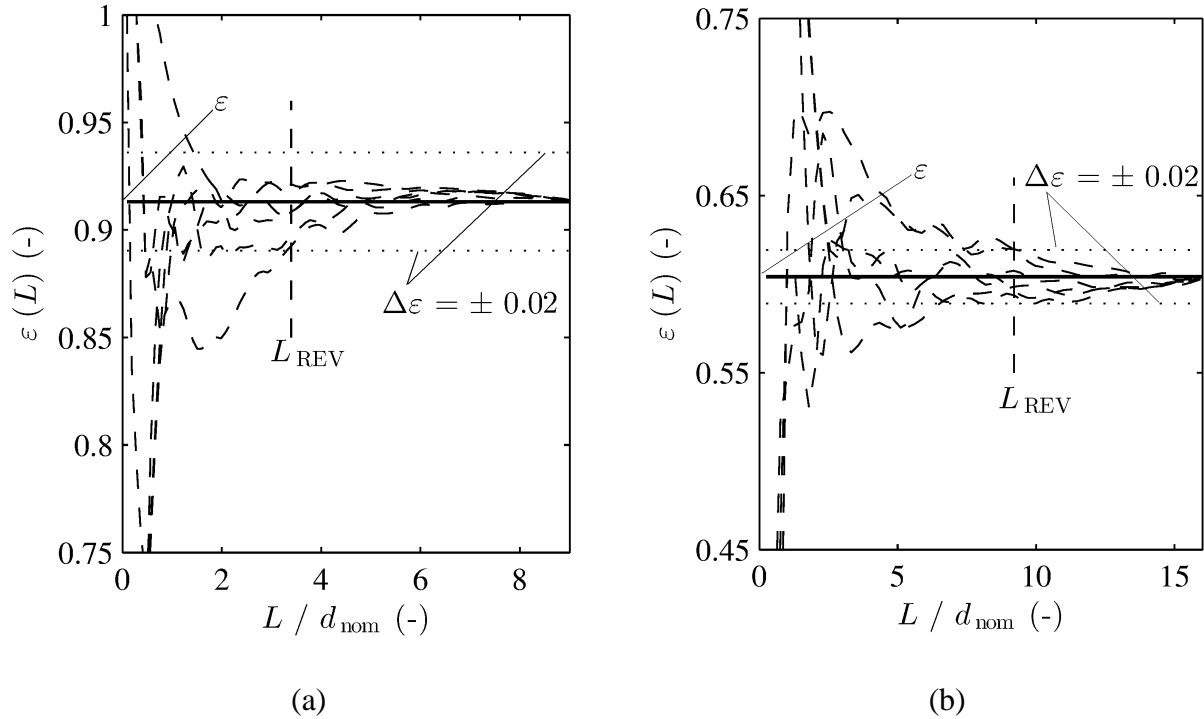


Figure 1-1. Representative Elementary Volume calculations of original samples for a) RPC, $\varepsilon = 0.913$ and b) CaCO_3 , $\varepsilon = 0.604$.

Table 1-1. Tomography data for model media.

Material	Sample size in voxels	Sample size (mm^3)	Δ (mm)	σ_k (mm)	Δ_k (mm)	$L_{\text{REV},05}$ (mm)	d_{nom} (mm)
RPC	768×768×768	23.04×23.04×23.04	0.030	1.5 Δ	5 Δ	8.9	2.54
CaCO_3 packed bed	512×512×512	23.04×23.04×23.04	0.045	1.5 Δ	5 Δ	5.4	1.41

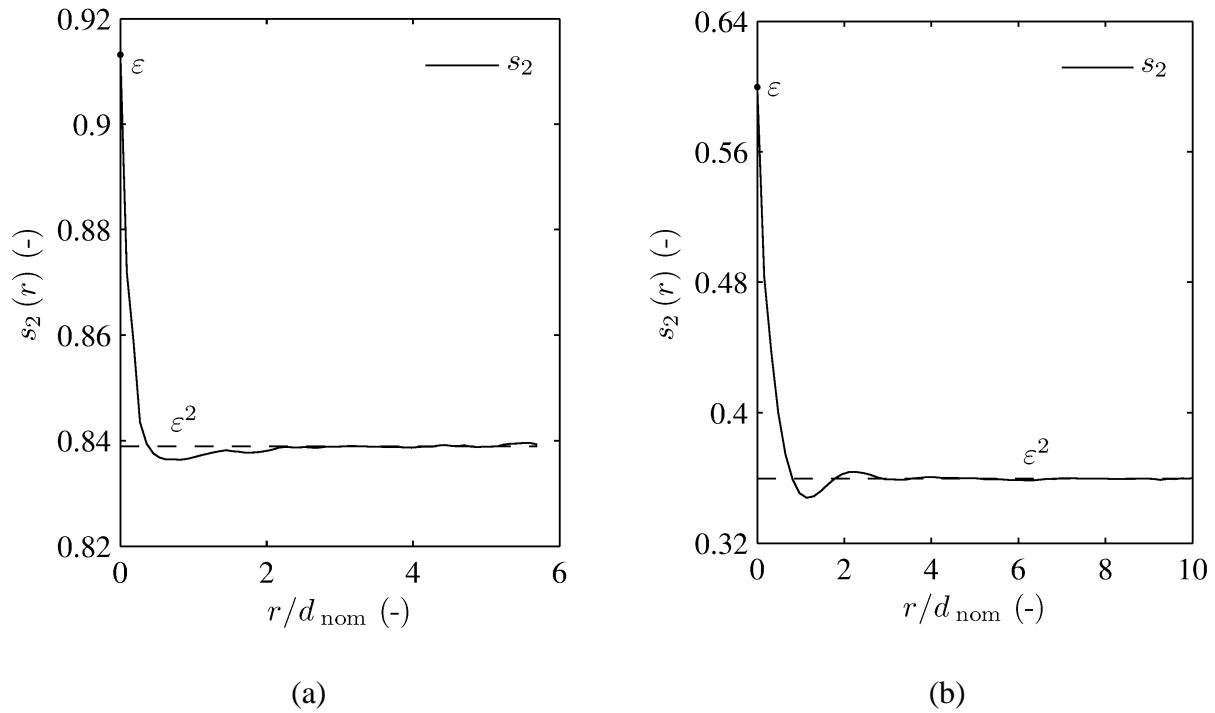


Figure 1-2. 2-point correlation functions of original samples for a) RPC, $\varepsilon = 0.913$ and b) CaCO_3 , $\varepsilon = 0.604$.

1.2.2 Manipulating Tomography Datasets

1.2.2.1 Removing noise and meso-porosity

Original sample tomography data contains grayscale noise which can cause significant error in calculation of the interface gray value ψ_0 as well as distort the morphology representation. In case of the RPC, hollow struts present in the solid matrix structure [17] are a significant source of meso-scale porosity which affects the outcome of morphological addition/subtraction operations. To remove these sources of error, iterative *openings* and *closings* [14] are performed on the images prior to segmentation.

1.2.2.2 Erosions and dilations to simulate porosity variation

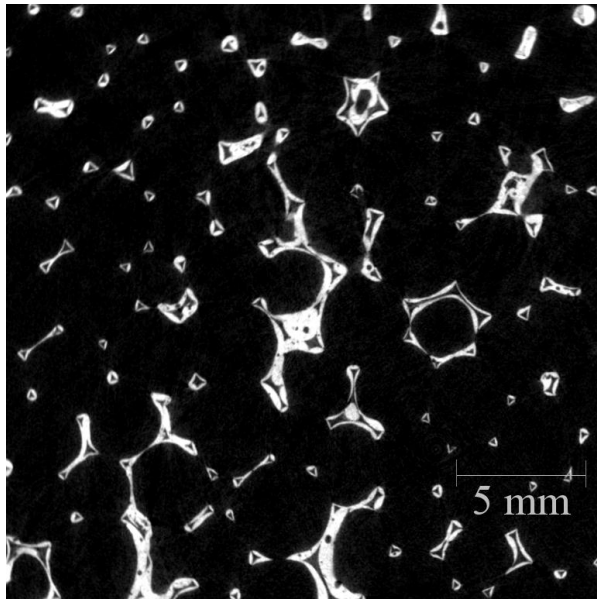
The addition of material to the solid phase and subtraction of material from it is simulated using *erosions* and *dilations* on the binary datasets prior to Gaussian filtering. These are

implemented using a 2-D, isotropic, disc structuring element of incrementally varying size on each of the N_z images in the datasets for the media. Since the medium is initially isotropic and erosions and dilations are Minkowski set operations, in which the structuring element behaves as a vector positioned at the interfacial pixels, the isotropy of the medium in 3-D is retained after image manipulation. Erosions cause reduction in the white ($\psi_{(\text{bin}),ijk} = 1$) region of the image, i.e. result in removal of a small layer from the solid phase, thus increasing the porosity, whereas dilations augment it, reducing the porosity. For the RPC sample, each dilation/erosion step corresponds to addition/removal of a layer of material 24 μm thick. Correspondingly, for the CaCO_3 sample, the rate of change of thickness is 45 μm per operation. In case of the CaCO_3 particle packed bed, since there is no significant connectivity between the particles, subsequent erosions will lead to disconnected particles typical for a fluidized bed. Figures 1-3 and 1-4 show samples of the image manipulation applied to each of the media.

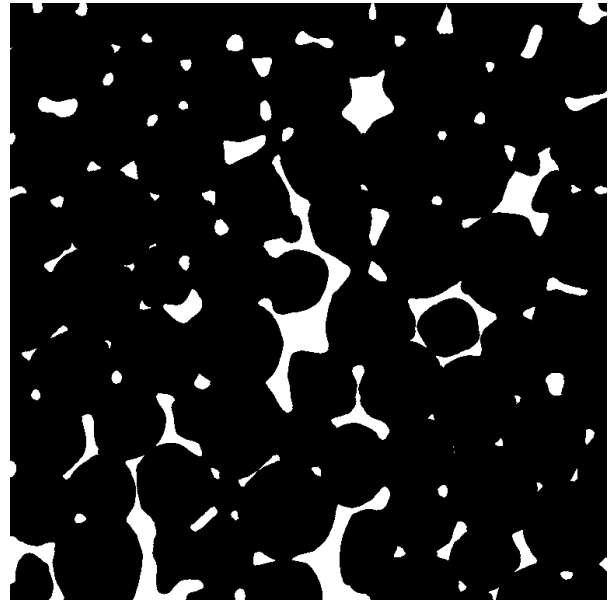
With the image processing routines applied, 20 sample volumes of the RPC, with porosity varying from 0.727 to 0.969 were generated and 25 sample volumes of the CaCO_3 particle packed bed with porosities between 0.134 and 0.918. Figure 1-5 shows the variation of specific surface area in the resulting samples.

It is clear from the description of the process that to simulate small thickness steps, either a very small disc size may be used (not recommended). A better way to simulate this change is by first expanding the image (using nearest neighbor interpolation) and then using a sufficiently large disc size so that circular symmetry is retained. Then the image is again reduced to the normal size again using the nearest neighbor interpolation.

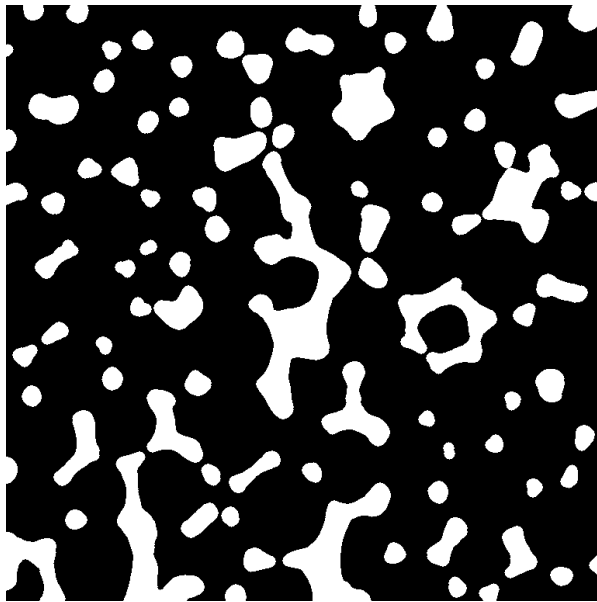
The disc element use is justified as long as the operations are performed on a larger image set of which the chosen dataset is a subset.



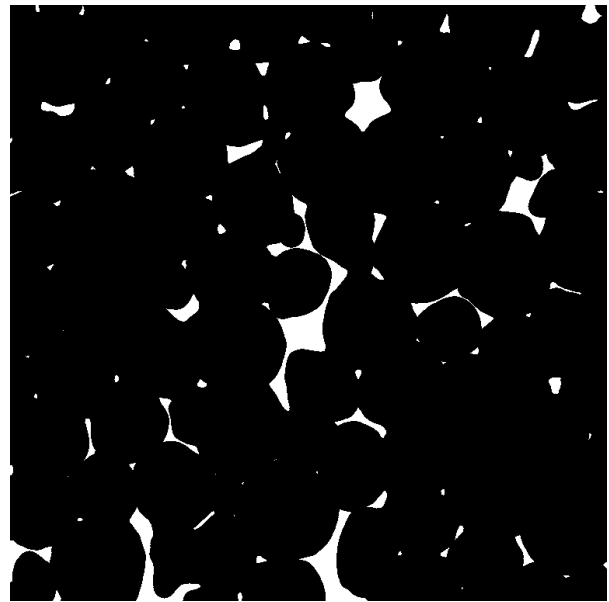
(a)



(b)

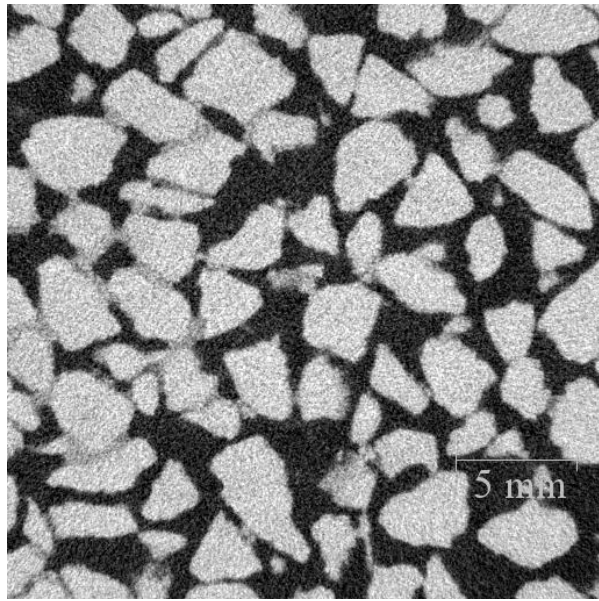


(c)

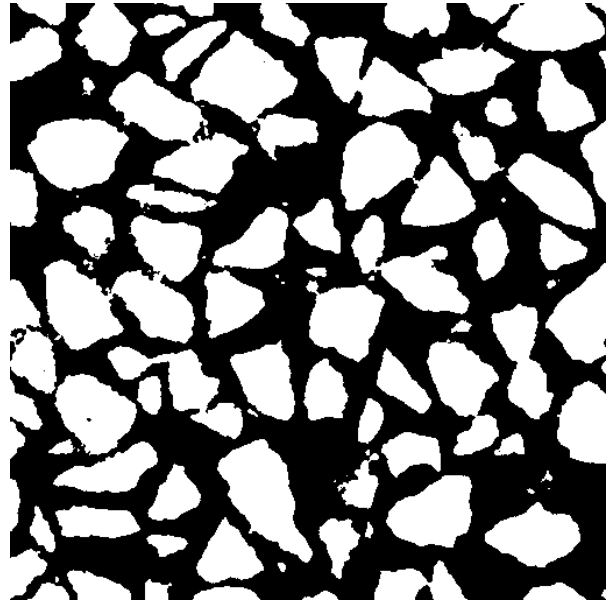


(d)

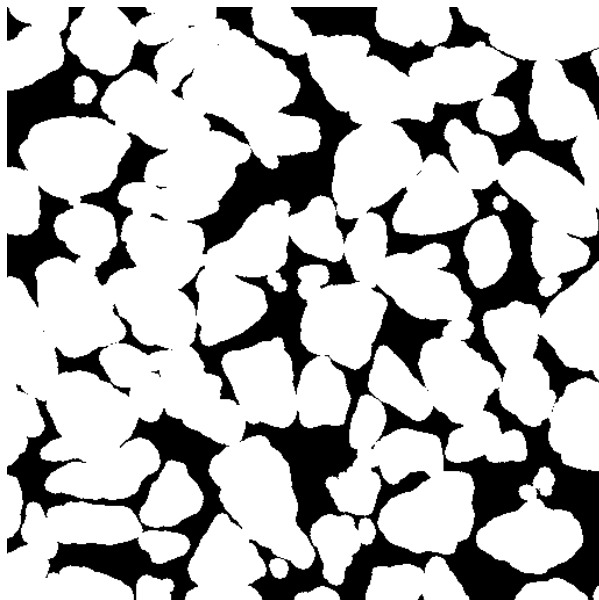
Figure 1-3. Morphological operations performed on RPC: (a) segmented sample image obtained from original tomography data, (b) image after iterative openings and closings to remove meso-scale porosity, (c) after addition of a layer 144 μm thick (d) after removal of a layer 120 μm thick.



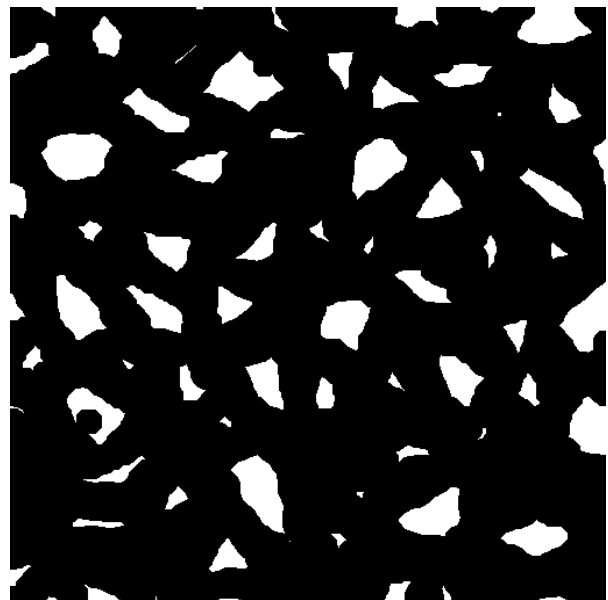
(a)



(b)



(c)



(d)

Figure 1-4. Morphological operations performed on tomography data for the packed CaCO_3 particle bed: (a) original data, (b) after segmentation and openings to remove noise (c) after addition of a layer 225 μm thick, (d) after removal of a layer 180 μm thick.

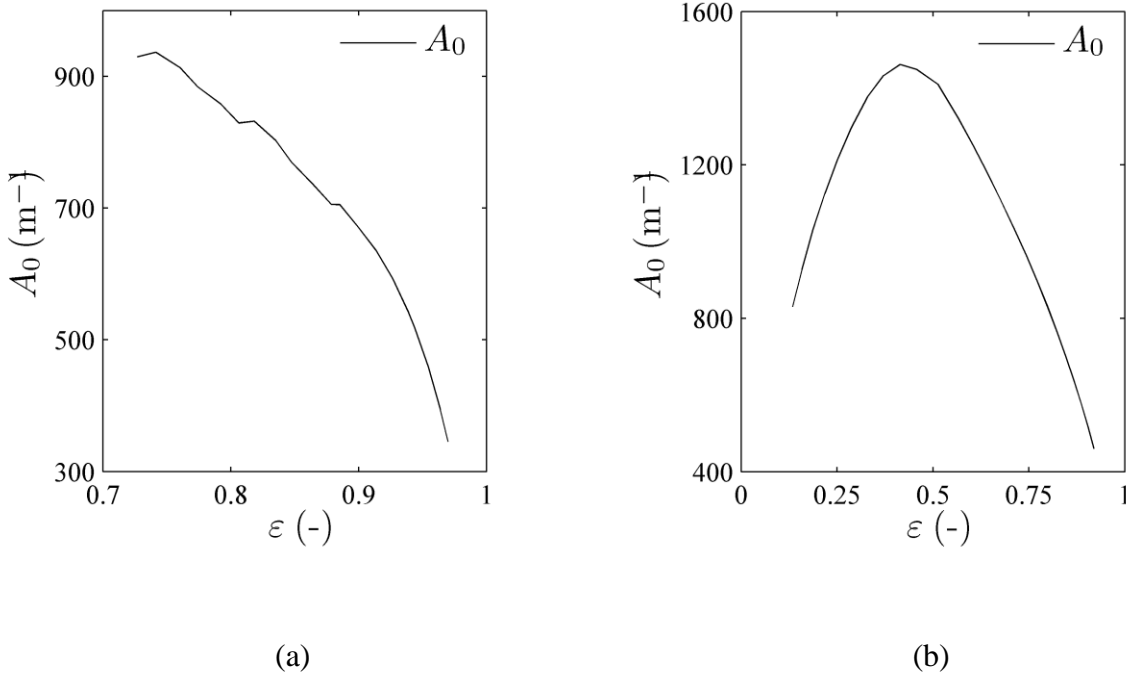


Figure 1-5. Specific surface area vs. porosity for a) RPC and b) CaCO₃ samples.

1.3 Summary

Porous media have a wide range of engineering applications, many of which require accurately determined effective transport properties of the media. Experimental determination of these properties is limited by manufacturability of graded samples of the media and inaccuracies in experimental data-collection, while analytical modeling delivers wide-ranging but inaccurate results due to underlying simplifications. High-resolution computer tomography data applied towards accurately capturing morphological information of porous media for use in numerical simulation of heat transfer phenomena has emerged as a feasible solution. This study extends the techniques for tomography-based property determination towards parameter-based characterization of transport properties. This is made possible by the use of image processing routines of *opening*, *closing*, *erosion*, and *dilation* through an isotropic 2-D structuring element,

to simulate porosity variation. A wide variation in sample porosity and specific surface can be achieved while still retaining the morphological characteristics unique to the medium.

CHAPTER 2 RADIATIVE HEAT TRANSFER *

2.1 Radiative Transfer in Porous Media

Radiative transfer in micro-structured porous media occurs in a range of technical applications such as porous radiant burners [4,18], packed beds or suspensions of reactive particles (e.g., in coal gasification and cracking of natural gas [6,7]), high temperature processes involving porous catalyst carriers [19], volumetric radiation receivers for solar thermal and solar thermochemical applications [8,20], etc. Design and optimization of microstructured materials require the accurate modeling of the effect of pore-level geometry on radiative transfer. Two approaches are conceivable: 1) using analytical models linking pore level geometry to radiative continuum properties and subsequently solving the radiative transfer equation (RTE) on the continuum level; and 2) direct pore level simulation of radiative transfer. The former approach involves using theoretically determined radiative properties of porous media [21] or incorporating reference measurements [22–24]. The latter approach, has been implemented via analytical approximations of porous media geometries [7,25–28], or the use of actual pore-level geometrical data from computer tomography [15,16,29], paired with MCRT [30–32]. Baillis et al. [21] describe techniques for the determination of thermal radiative properties of porous or disperse media. Nisipeanu et al. [33] provide a comparative study of continuum and direct simulations of radiative transfer. Petrasch et al. [34] have numerically demonstrated the equivalence of continuum and direct modeling for certain materials.

Efforts to identify and improve application specific radiative properties of porous media have been previously conducted both experimentally [35] and through theoretical models [36]. In

* Material from this chapter has been published in: A. Akolkar, J. Petrasch, Tomography based pore-level optimization of radiative transfer in porous media, *International Journal of Heat and Mass Transfer*. 54 (2011) 4775–4783.

solar thermochemical processing [8] and volumetric solar thermal receivers [20], porous absorbers need to have high absorptance for maximum energy collection. The present study applies tomography-based methods to analyze and optimize the overall absorptance of slabs of the model media described in chapter 1. It is assumed that the media are non-homogeneous, two-phase materials, with one phase (void) completely transparent and the other phase (solid) completely opaque and gray. Both phases are assumed to be isothermal and the medium temperature is low, i.e., the contribution of emission from within the medium to radiative intensity is negligible compared to that of the irradiating source [15,27,29]. Geometric optics is valid. Only surface exchanges are considered in the MCRT model.

In this chapter, the effect of varying pore-level geometry, via addition and removal of material, on the absorptance of slabs subjected to direct radiation, is studied. Further, the effect of surface reflectivity and directional distribution of incident radiation (collimated/diffuse) is studied. Diffuse and specular reflections are considered as the limiting cases for the directional surface characteristics. Then, a parametric two-flux model is fitted onto the direct simulation data. Values of the extinction coefficient, forward scattering fraction and asymmetry factor [32] are calculated for each of the cases above. The model is used to optimize porous slabs for absorption. Optimum porosities increase with sample thickness. For given relative sample thicknesses the optimum porosity for RPCs is seen to be much higher than for CaCO₃ bed.

2.2 Methodology

The process of generating samples of varying porosity from the original tomography data has been discussed in chapter 1. Samples thus generated are used in MCRT simulations. The surface reflectivity and sample thickness along irradiated direction are treated as parametric values in the simulations.

For this study, we consider $L_{REV, 0.05}$ sufficiently accurate. The pore space is also quantified by the nominal pore diameter, d_{nom} . For the RPC, the pores per inch (ppi) define d_{nom} whereas for the CaCO_3 particle packed bed sample d_{nom} is the hydraulic diameter at $\varepsilon = 0.5$. The relevant values have been given in chapter 1, table 1-1. Thickness variation in samples is simulated in steps of d_{nom} by simply selecting the appropriate numbers of voxels in the irradiated direction when computing MCRT results.

Among the simplifying assumptions used in the MCRT setup is independent scattering [32]. The smallest geometrical feature resolved is of the size of one voxel. The size parameter based on the size of one voxel, $\xi_{\Delta} = \Delta/\lambda$, is 62.5 for the RPC and 93.75 for the CaCO_3 particle packed bed, for a wavelength $\lambda = 500$ nm. In this case, Figure 11-2 in [32] justifies neglecting dependent scattering even for very small porosities. The following sections describe the MCRT model used, boundary conditions and the analytical model development.

2.2.1 The Monte Carlo Method

Non-energy partitioning [37] Monte Carlo ray tracing is employed to study the interaction of radiation with the model media. A large number (10^6) of stochastic ray paths are generated on a parallel plane just outside the sample volume. Incident radiation is either collimated or diffuse. Surfaces may either be diffuse or specularly reflecting. For a specularly reflecting surface, the directional hemispherical reflectivity is calculated using an approximate expression for Fresnel's equation [27] ,

$$\rho'(\theta_i) = 1 - \frac{3}{2} \alpha \cos(\theta_i) \quad (2-1)$$

where θ_i is the angle of incidence of the ray on the surface and α is the hemispherical absorptivity.

The point of incidence of a ray with a starting point \mathbf{P}_0 and direction $\hat{\mathbf{s}}$ on the solid phase is calculated by

$$\Psi(\mathbf{P}_0 + s\hat{\mathbf{s}}) - \psi_0 = 0 \quad (2-2)$$

where s is the distance travelled from the starting point to the interface and ψ_0 is the interface gray value. At the solid surface, whether the ray is reflected or absorbed is determined by comparing a uniform random number with the reflectivity [32]. The surface normal is calculated as the normalized gradient of the Gaussian smoothed continuous gray level function [13,15],

$$\hat{\mathbf{n}}(\mathbf{P}_i) = \frac{\nabla\Psi|_{\mathbf{P}_i}}{|\nabla\Psi|_{\mathbf{P}_i}} \quad (2-3)$$

where \mathbf{P}_i is the point of incidence of the ray.

The history of each ray is recorded until it is either absorbed or exits the sample. Absorptance, reflectance, and transmittance of the slab are then calculated accordingly. Separate simulations are carried out for all six entry planes to average out the statistical fluctuations.

A perfectly reflecting, specular boundary condition is assumed at the four faces parallel to the direction of incidence [13,30], thus simulating an infinite slab. Figure 2-1 depicts the simulated situation. Figure 2-2 shows the points of reflection on a sample of the RPC of porosity 0.913 with a specular solid phase surface, reflectivity 0.65, under the simulation conditions with diffuse irradiation of the sample. It can be seen in the figure 2-2 that the incoming radiation fails to penetrate significantly through to the end of the sample. Also, the density of reflected rays decreases along the sample thickness. For diffuse radiation, the probability of grazing rays from the specular solid phase being reflected back is higher than for collimated radiation. This causes the peculiar pattern.

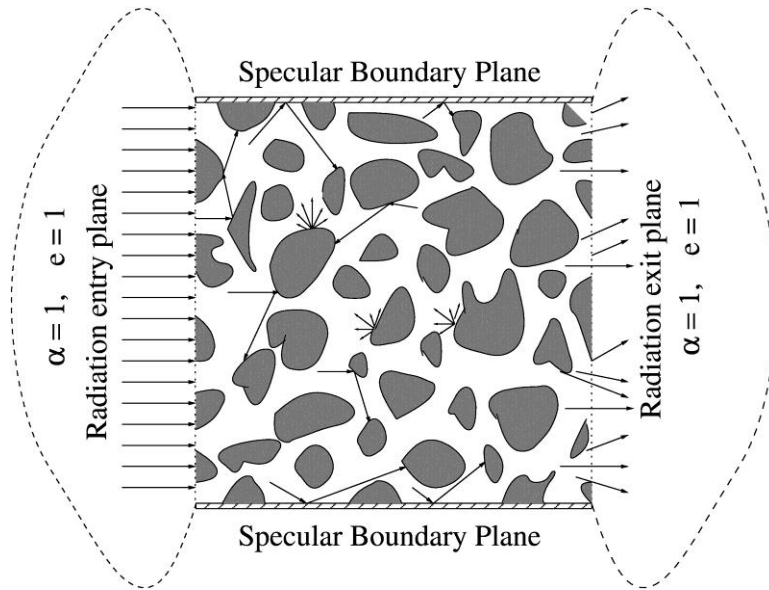


Figure 2-1. Simulated system and boundary conditions

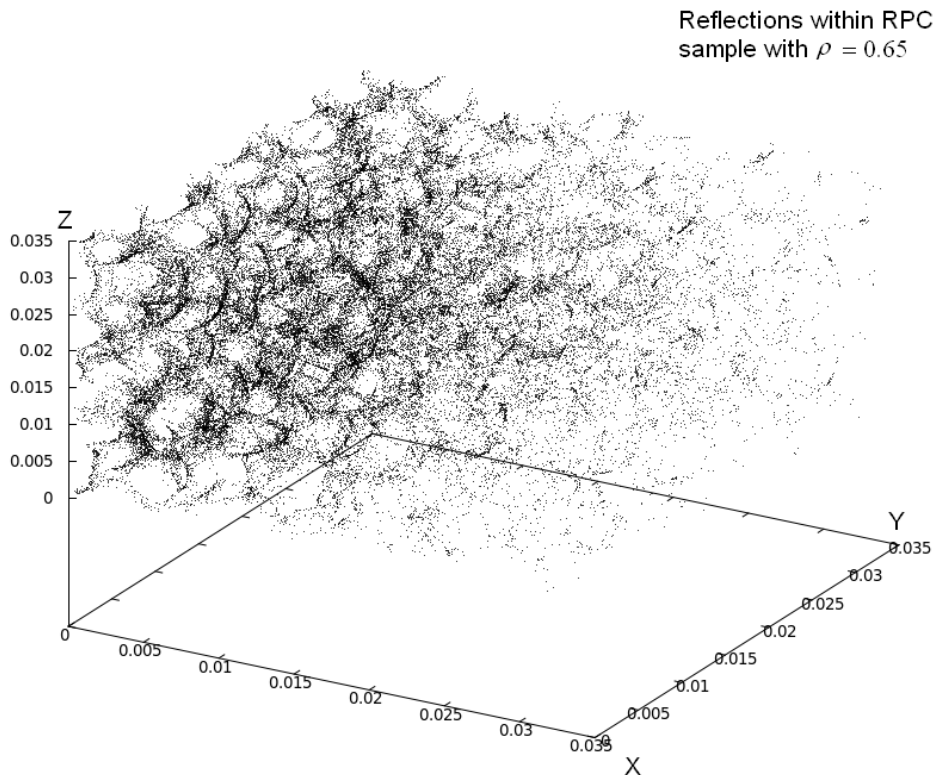


Figure 2-2. Surface reflections in RPC sample of $\varepsilon = 0.913$ at $\rho = 0.65$, with specular surfaces. Notice the penetration of radiation in the irradiated direction (+X). Even at high porosity, the transmission through the sample is low.

2.2.2 Analytical Model

A two-flux model analogous to the modified Schuster-Schwarzschild approximation used by Sagan and Pollack [38] is used. For purely absorbing and scattering media with unbalanced forward-backward scattering, the following set of linear differential equations is obtained:

$$\begin{aligned}\frac{dI^+}{dx} &= -\beta I^+ + \sigma_s \left(kI^+ + (1-k)I^- \right) \\ \frac{dI^-}{dx} &= \beta I^- - \sigma_s \left(kI^- + (1-k)I^+ \right)\end{aligned}\tag{2-4}$$

where I^+ and I^- are normalized intensities in the forward and backward hemispheres of the sample, respectively; β is the *extinction coefficient* and k is a *forward scattering fraction*. For geometric optics, according to [32], the scattering coefficient is:

$$\sigma_s = \rho \beta\tag{2-5}$$

A geometric optics model for the extinction coefficient developed by Hsu and Howell [39] by modeling a porous ceramic as a suspension of monodispersed, independently scattering spherical particles, and as used by Hendricks and Howell in [40] is used:

$$\beta = \frac{c}{d_{\text{nom}}} (1 - \varepsilon)\tag{2-6}$$

where ρ is the hemispherical reflectivity and c is a correlation constant. The general solution of Eq. 2-4 is:

$$\begin{pmatrix} I^+ \\ I^- \end{pmatrix} = q_1 \mathbf{V}_1 e^{\gamma_1 x} + q_2 \mathbf{V}_2 e^{\gamma_2 x}\tag{2-7}$$

The eigenvalues γ are given by:

$$\gamma_{1,2} = \mp \left(\beta \sqrt{1 - 2k\rho + \rho^2 (2k - 1)} \right)\tag{2-8}$$

which yield the rate of change in intensity. The eigenvectors $\mathbf{V}_{1,2}$ are given by:

$$\mathbf{V}_{1,2} = \begin{pmatrix} \frac{(2-k\rho) \pm \sqrt{(\rho-1)(2k\rho-\rho-2)}}{(1-k)\rho} \\ 1 \end{pmatrix} \quad (2-9)$$

Finally, the constants of integration, q_1 and q_2 , are obtained by applying the following boundary conditions:

$$\begin{aligned} I^+(x) \Big|_{x=0} &= \varepsilon \\ I^-(x) \Big|_{x=L} &= 0 \end{aligned} \quad (2-10)$$

where L is the sample length selected. Transmittance, T , and reflectance, R , are then obtained as:

$$\begin{aligned} T &= I^+(x) \Big|_{x=L} \\ R &= (1-\varepsilon)\rho + I^-(x) \Big|_{x=0} \end{aligned} \quad (2-11)$$

with ρ being the hemispherical reflectivity at the sample face plane. Finally, the absorbance of the material sample is simply given as:

$$A = (1 - R - T) \quad (2-12)$$

The Schuster-Schwarzschild approximation does not assume a specific phase function. However, a binary, asymmetric scattering phase function ($\Phi(\mu)$) defined below using the forward scattering fraction and the Dirac Delta function (δ) is consistent with the model:

$$\Phi(\mu) = 2[k\delta(\mu-1) + (1-k)\delta(\mu+1)] \quad (2-13)$$

where μ is the cosine of the scattering angle, θ_s and Φ is assumed to be independent of the azimuthal angle, φ . Using this, the asymmetry factor [32], or scattering anisotropy factor is calculated as,

$$g = \overline{\cos \theta_s} = \frac{1}{4\pi} \int_{4\pi} \Phi(\theta_s) \cos \theta_s d\Omega = 2k - 1 \quad (2-14)$$

with $\mu = \cos \theta_s$.

Then, the unknowns, c and k , are obtained via least square fitting of the model output (Eq. 2-11) onto direct numerical simulation results for transmittance and reflectance using the L/d_{nom} ratio, sample porosity, ε , and the hemispherical reflectivity, ρ , as parameters. For the media given, we have used 16 values of thicknesses (RPC: $0.57 < L/d_{\text{nom}} < 9.1$, CaCO_3 particle packed bed: $1.21 < L/d_{\text{nom}} < 19.4$) and have varied the hemispherical reflectivities from 0.45 to 0.9. The data contains 20 values of porosity ($0.73 < \varepsilon < 0.97$) for the RPC and 25 values of porosity ($0.13 < \varepsilon < 0.92$) for the CaCO_3 particle packed bed sample.

2.2.3 Convergence Study

A convergence study is carried out for the RPC and the CaCO_3 particle packed bed sample, with a diffuse solid phase and of reference porosity $\varepsilon = 0.8351$ for the RPC and $\varepsilon = 0.4577$ for the CaCO_3 particle packed bed, with $\rho = 0.65$ for 10^3 , 10^4 , 10^5 , 10^6 , 10^7 , and 10^8 stochastic rays. The relative change in values of absorptance and reflectance with increased number of irradiating rays is depicted in the figure 2-3. Here,

$$A_{\text{rel}} = \frac{|(A_{N_{\text{rays}}} - A_{10^8})|}{A_{10^8}} \quad (2-15)$$

$$R_{\text{rel}} = \frac{|(R_{N_{\text{rays}}} - R_{10^8})|}{R_{10^8}}$$

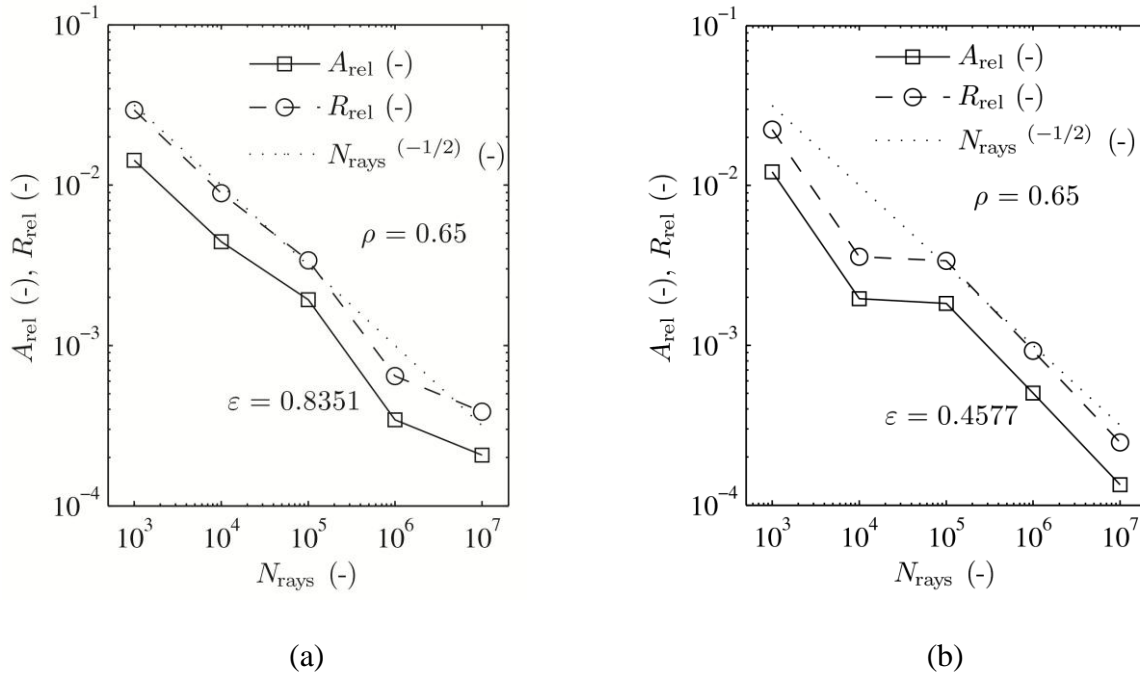


Figure 2-3. MC convergence study for an RPC sample of porosity $\varepsilon = 0.8351$ and a CaCO_3 packed particle bed sample of porosity $\varepsilon = 0.4577$ for diffuse surfaces, irradiated with diffuse radiation.

Since MCRT is a statistical method, the convergence for the MC shows significant fluctuations for some runs. As indicated by the trend line for $N_{\text{rays}}^{-1/2}$, the convergence follows the Central Limit Theorem. The convergence error at 10^6 rays is well below 0.001 for both cases, and this is below the tolerance on the L_{REV} . Therefore, a maximum likelihood estimation of the extinction correlation coefficient and the forward scattering fraction was not considered and the results were accepted as accurate within the limits of the stochastic geometry fluctuations.

2.3 Results

Transmittance and reflectance are plotted for diffuse and collimated incident radiation, for diffuse and specular solid phases; for the RPC and the CaCO_3 particle packed bed as a function of sample thickness. In each case, the maximum sample dimensions are $23.04 \text{ mm} \times$

23.04 mm × 23.04 mm and the sample thickness is varied along the normal to the irradiated plane.

Figure 2-4 shows the variation of transmission and reflectance with the L/d_{nom} ratio, in the case of a diffusely irradiated RPC sample volume, with the hemispherical reflectivity of the solid phase, $\rho = 0.65$, for the case of both diffuse (fig. 2-4(a)) and specular (fig. 2-4(b)) solid phases. For samples of low and moderate porosity, the transmittance becomes negligible at lengths approaching $6d_{nom}$. However, it remains comparable to the reflectance for highly porous ($\varepsilon=0.96$) samples. The above value of ρ is chosen to represent the average spectral behavior of a variety of sample media.

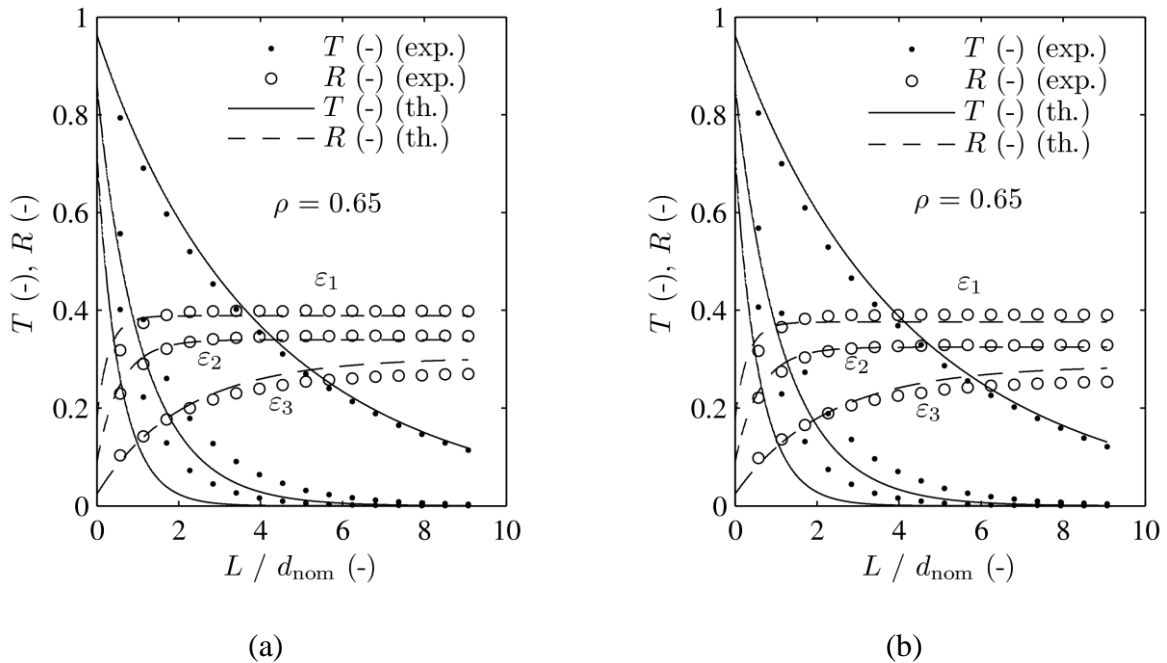


Figure 2-4. Transmittance and reflectance for diffusely irradiated RPC sample, in case of (a) diffuse solid phase (b) specular solid phase. Here, $\varepsilon_1 = 0.727$, $\varepsilon_2 = 0.863$, $\varepsilon_3 = 0.964$.

Table 2-1 summarizes the correlation coefficient and the forward scattering fraction for the cases considered in this paper. From figure 2-4 and table 2-1, for the specular solid phase, the

value of the correlation coefficient, c , is lower. At the same time, the forward scattering fraction k takes a larger value, indicating greater forward propagation of radiation. Hendricks and Howell [40] have predicted c for RPCs as 4.4, Petrasch [13] has experimentally and tomographically determined c as 5.5 for a specific RPC sample. The difference presented here is attributed to the wider range of porosities considered and the limits of the 1D 2-flux method.

Figure 2-5 and table 2-1 give RPC results for collimated radiation. The extinction correlation coefficient is smaller than in case of diffuse irradiation. A diffuse solid phase again tends to cause more radiation to be back than a specular phase. However, overall, the RPC behaves as a better absorber of collimated radiation than of diffuse radiation at typical porosities.

Table 2-1. Extinction correlation coefficient, c , forward scattering fraction, k , and asymmetry factor, g , for the media studied

Medium	Irradiation	Solid phase	c (-)	k (-)	g (-)	$RMSE$ (-)
RPC	Diffuse	Diffuse	9.561	0.379	- 0.243	5.11×10^{-4}
		Specular	9.482	0.444	- 0.113	5.14×10^{-4}
	Collimated	Diffuse	7.126	0.487	- 0.026	5.77×10^{-4}
		Specular	7.0326	0.574	0.148	6.51×10^{-4}
CaCO ₃ particle packed bed	Diffuse	Diffuse	2.783	0.608	0.217	1.40×10^{-4}
		Specular	2.742	0.643	0.286	1.76×10^{-4}
	Collimated	Diffuse	2.199	0.694	0.384	2.28×10^{-4}
		Specular	2.143	0.721	0.441	2.72×10^{-4}

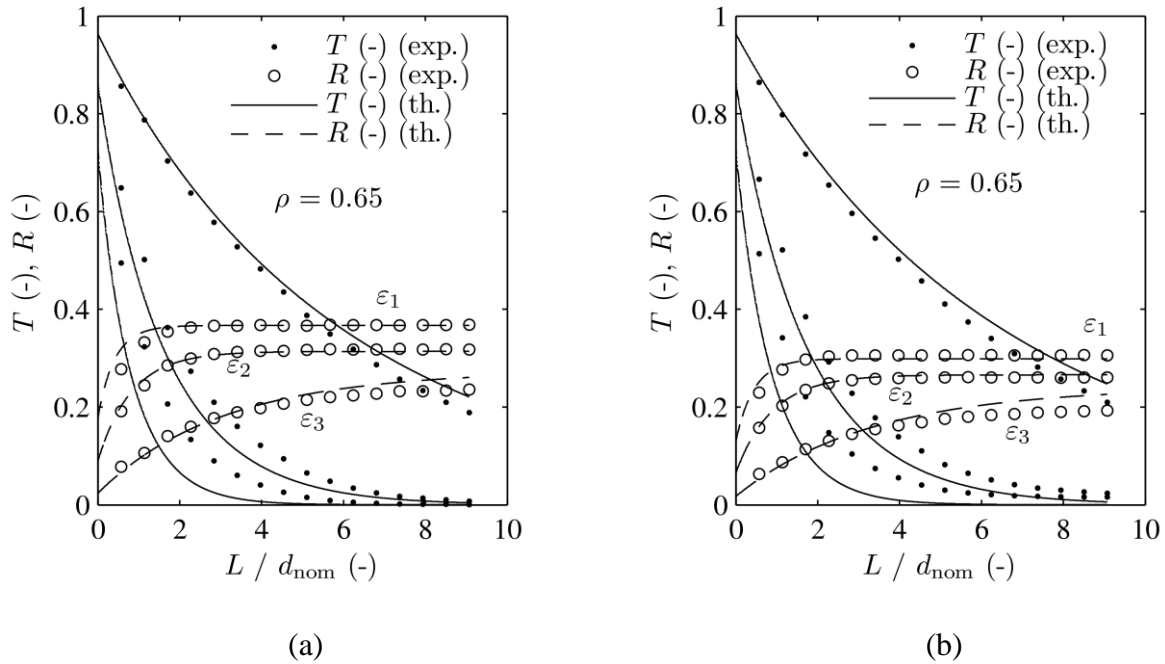


Figure 2-5. Transmittance and reflectance for RPC sample irradiated with collimated radiation, in case of (a) diffuse solid phase (b) specular solid phase. Here, $\epsilon_1 = 0.727$, $\epsilon_2 = 0.863$, $\epsilon_3 = 0.964$.

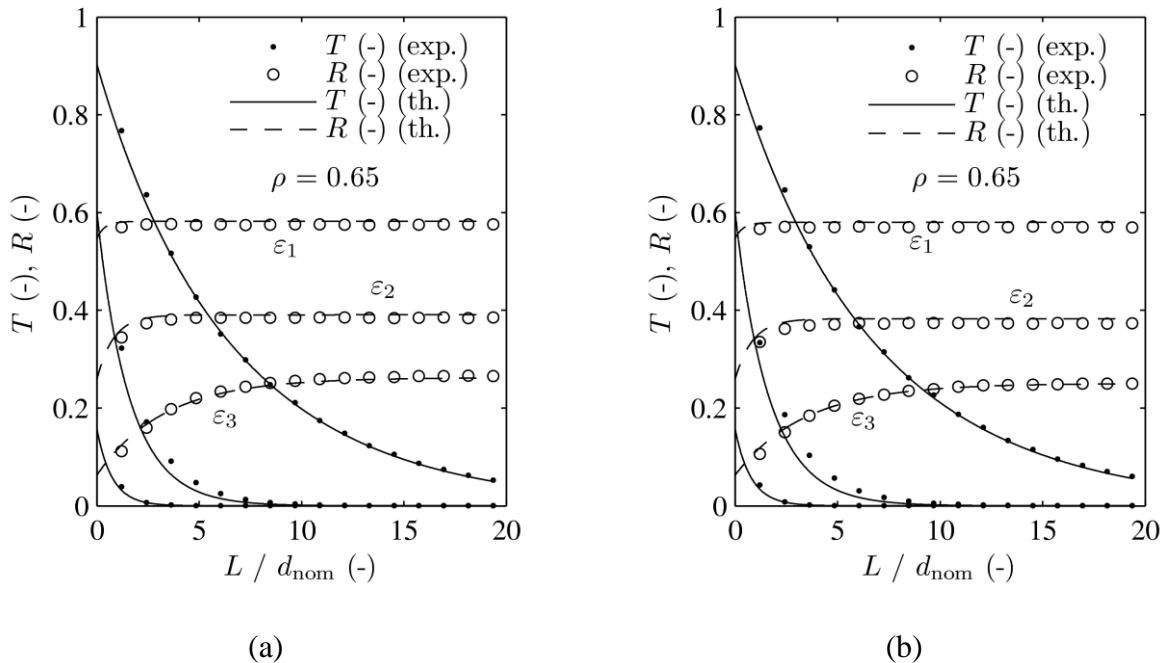


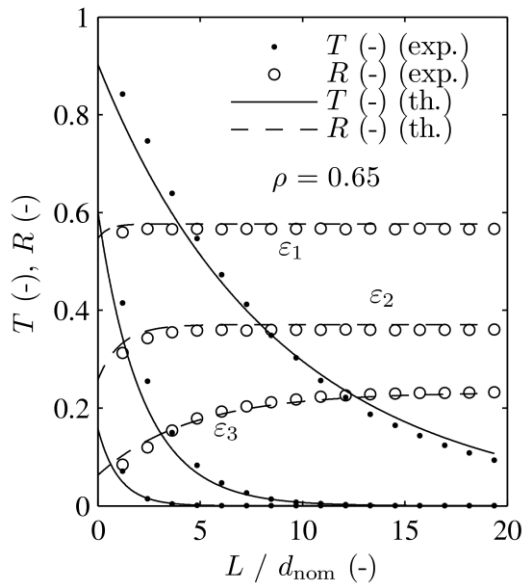
Figure 2-6. Transmittance and reflectance for CaCO_3 particle packed bed sample irradiated with diffuse radiation, in case of (a) diffuse solid phase (b) specular solid phase. Here, $\epsilon_1 = 0.159$, $\epsilon_2 = 0.604$, $\epsilon_3 = 0.904$.

The packed bed of CaCO_3 particles exhibits a higher overall transmittance for a given porosity than the RPC. The extinction correlation coefficient is smaller than that of the RPC. Figure 2-6 gives results for the packed CaCO_3 particle bed subjected to diffuse radiation.

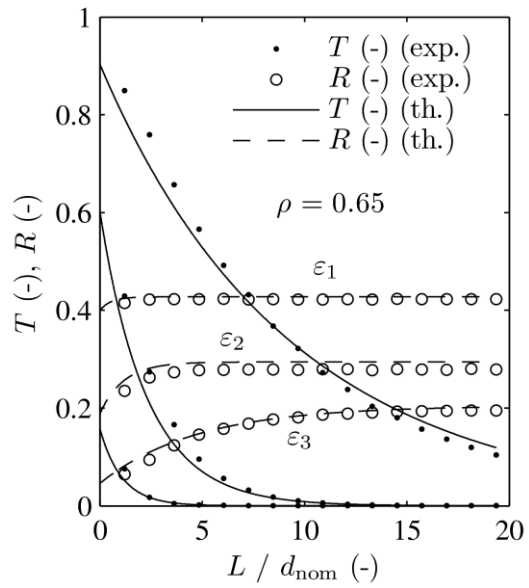
The difference in the behaviors of the CaCO_3 particle packed bed and the RPC can be explained by the geometry of the solid phases. The RPC consists of a highly connected, finely structured geometry. This yields a large surface to volume ratio in the solid phase. This is not the case with the CaCO_3 particle packed bed, which features a disconnected solid phase with a much lower surface to volume ratio for a comparable porosity. This allows radiation to be ‘trapped’ within the RPC structure, with more reflections per ray within a given volume as compared to the CaCO_3 particle packed bed. This, in turn, enhances the probability of absorption of radiation within the RPC volume.

Table 2-1 and figure 2-7 give results for the CaCO_3 particle packed bed irradiated with collimated radiation. As in the case of the RPC, the sample performs better if exposed to collimated radiation. The CaCO_3 particle packed bed has a higher value of k than the RPC, indicating a stronger tendency to scatter radiation forward. Therefore, larger sample L/d_{nom} ratios are required for optimal performance of the CaCO_3 particle packed bed as an absorber.

Maximization of the absorptance of finite thickness media samples is carried out based on the two-flux model introduced in section 3. Figure 2-8 shows the results of the optimization process for diffuse radiation on a diffuse solid phase, in the case of the RPC and the packed bed of CaCO_3 particles respectively. Absorptance is shown as a function of sample L/d_{nom} ratio and porosities.

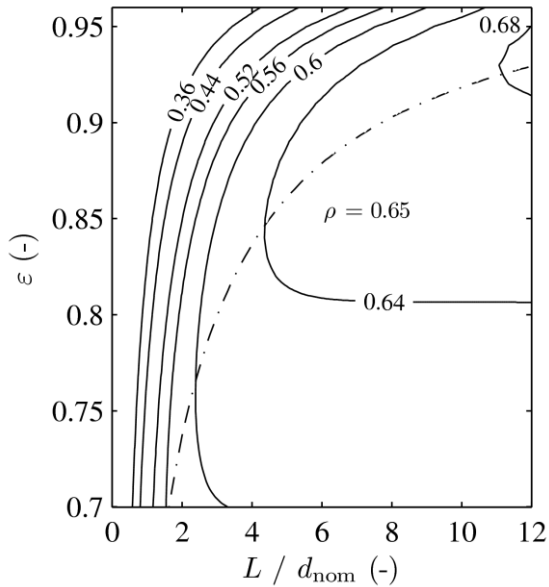


(a)

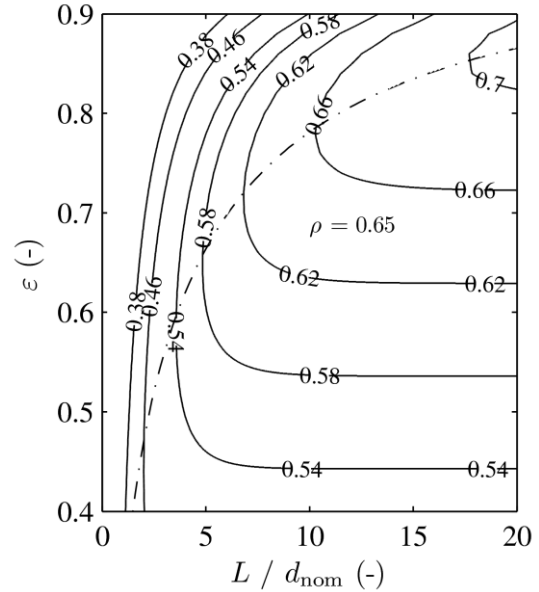


(b)

Figure 2-7. Transmittance and reflectance of CaCO_3 particle packed bed for sample irradiated with collimated radiation, in case of (a) diffuse solid phase (b) specular solid phase. Here, $\varepsilon_1 = 0.159$, $\varepsilon_2 = 0.604$, $\varepsilon_3 = 0.904$.



(a)



(b)

Figure 2-8. Absorptance RPC (a) and CaCO_3 particle packed bed (b), for diffuse radiation and diffuse solid phases, with solid phase $\rho = 0.65$. The dotted line indicates the local optimal porosity as a function of L/d_{nom} .

Figure 2-8 indicates that optimum porosities increase with sample thickness. Also, the CaCO_3 particle packed bed sample is less efficient as an absorber for comparable porosities and sample lengths than the RPC.

2.4 Summary

This study extends the direct pore level simulation approach used in [15,16] to optimizing the micro-geometry of porous structures for radiative performance. Representative samples of a disconnected solid-phase medium (a packed bed of CaCO_3 particles) and connected solid-phase medium (an RPC) are studied. Image processing concepts of dilation and erosion are utilized to simulate a stepwise change in medium porosity. A two-flux model, based on a modified version of the Schuster-Schwarzschild approximation has been applied to characterize the medium radiative behavior.

Results obtained from the model were in good agreement with the simulation data, with a maximum RMS error of 0.0006 across all cases examined. The MC model exhibited steady convergence.

The extinction coefficients for the RPC are seen to be higher than for the packed CaCO_3 particle bed. Also, the RPC has a lesser tendency for forward scattering of radiation as compared to the CaCO_3 particle packed bed sample. Thus, for the packed particle bed to perform as a good absorbing medium, a larger sample thickness will be required than that for an RPC sample of comparable porosity and solid phase reflectivity.

While the results provided in this paper do not cover the entire range of pore-level geometries in the model media, they make a strong case for tailoring their porosities to develop optimum absorber structures. They are also applicable to the continuum modeling and design of these media. Medium porosities can be tailored to optimize for desired radiative behavior, by

carefully controlling the viscosity of ceramic slurry [12] in case of porous ceramics, or by managing the bed packing density and fluidization parameters in case of particle beds [36].

CHAPTER 3 FLUID FLOW *

3.1 Fluid Flow in Porous Media

The diverse engineering applications of porous media, such as particulate filters [10], structured catalytic media [9], volumetric radiation receivers for solar-thermal applications [8] etc., all exploit the heat and mass transfer characteristics peculiar to these media [3]. Fluid flow through porous media is of considerable interest in these applications [1].

The modeling of such microstructured media usually relies on volume averaged models [11]. These models typically require one or several effective transport properties, which in turn depend on the porous microgeometry. Various phenomenological, geometrical and statistical models to predict these transport properties exist [1,2,41]. Either conduit flow or drag flow, two opposite approaches of flow analysis, are typically employed in these models, with conduit flow models performing better at lower porosities and drag flow models performing better at higher porosities [2]. High resolution computer tomography in conjunction with direct pore-level numerical simulations (DPLS) [13] provides a rigorous and accurate alternative to these traditional empirical or statistical methods. The accuracy of permeabilities and Dupuit-Forchheimer coefficients determined by this method is only limited by the size of the tomographic dataset, its resolution and the discretization error of the numerical fluid solver employed.

Tomography data has been successfully used in determining medium permeabilities via random walk simulations [42], in Lattice-Boltzmann flow simulations [43], for creating pore-scale network models useful in transport simulations [44], for obtaining lineal path functions [45]

* Material from this chapter has been submitted for publication in: A. Akolkar, J. Petrasch, Tomography Based Characterization and Optimization Of Fluid Flow Through Porous Media, *Transport in Porous Media*, submitted March 2012.

etc. Characterization of overall convection heat transfer properties of RPCs using tomography based methods has been carried out in [13]; similar characterization of a packed particle bed has been done in [46].

With the use of image processing operations on tomography data, topology variation can be affected, thereby extending the results of numerical simulations over a wider range of chosen topological parameters such as porosity. This was demonstrated for thermal radiative transfer in [47] and is extended to fluid flow in the current work. Samples of incrementally varying porosity are created from tomography datasets of a 10 pores per inch (ppi) RPC and a packed bed of CaCO_3 particles respectively. Stationary 3-D, single phase fluid flow simulations with quasi 1D boundary conditions and Reynolds numbers ranging from 0.1 – 200 are carried out for each sample. The measured pressure gradient is used to calculate sample permeability and Forchheimer coefficient via fitting of a modified Darcy’s law [1,2]. Results are compared with traditional flow models. Models best suited to each medium are identified. An adjusted Kozeny constant is then calculated by fitting the Carman-Kozeny equation to the results across porosities, for either medium.

3.2 Theory

3.2.1 Darcy’s Law, Permeability and Dupuit-Forchheimer Coefficient

Darcy’s law [2] for macroscopic flow through an isotropic porous medium, is expressed as,

$$-\nabla p = \frac{\mu}{K} \mathbf{u}_D \quad (3-1)$$

Here, the pressure gradient (∇p) within the fluid phase is related to the mean fluid velocity (\mathbf{u}_D) (Darcean velocity) through the fluid viscosity, μ , and the permeability, K , the

fundamental property governing low-Re transport through porous materials. At higher average velocities, an additional quadratic term was proposed independently by Dupuit [48] and Forchheimer [49], to account for higher Re effects [2]. The one-dimensional modified Darcy equation is:

$$\nabla p = -\frac{\mu}{K} u_D - F \rho u_D^2 \quad (3-2)$$

where F is the Dupuit-Forchheimer coefficient.

The non-dimensionalized viscous pressure gradient,

$$\Pi_{pg} = \frac{\nabla p d^2}{\mu u_D} \quad (3-3)$$

can hence be expressed as a linear function of the flow Reynolds number by rewriting Eq. 3-2, as,

$$\Pi_{pg} = -c_0 - c_1 \text{Re} \quad (3-4)$$

Here, d is the fluid-flow characteristic length scale of the porous medium, (e.g. pore diameter), c_0 is the inverse dimensionless permeability, and c_1 is the dimensionless Dupuit-Forchheimer coefficient:

$$c_0 = \frac{d^2}{K}, \quad c_1 = dF \quad (3-5)$$

Hence the permeabilities and the Dupuit-Forchheimer coefficients can be determined based on numerical simulations of quasi-1D flow at multiple Reynolds numbers from the zero-offset and the slope of the best-fit line to Eq. 3-4. The method has been described in [50], it will be used to examine the applicability of a range of property models to porous structures with a wide range of porosities.

3.2.2 Analytical Flow Models

A number of geometrical and phenomenological flow models exist for predicting the permeability and Dupuit-Forchheimer coefficient (non-Darcy coefficient). Detailed reviews of these models have been provided in [1,2].

3.2.2.1 Models for permeability

Models of permeability are typically based on simplifying assumptions applied to the flow-path geometry. The two main classes of permeability models are conduit flow models (flow inside a channel) and drag flow models (flow around a submerged body) [2]. Both types of models rely on a simplified characterization of the medium topology via porosity, ε , and the specific surface area, A_0 . Empirical correlations generalizing results for a specific geometry and porosity range are limited in scope [1]. Geometric and semi-heuristic relationships typically have wider range of applicability but lower overall accuracy. As such, no universally applicable relationship in terms of the morphological parameters, ε and A_0 for predicting permeability exists [1]. In general, drag models are known to become less effective in permeability prediction with decreasing porosity, whereas conduit models become less effective at high porosities [2].

Conduit Flow – Hagen-Poiseuille relation: Considering an arrangement of parallel straight tubes of diameter d , and integrating the one-dimensional Navier-Stokes equation for the pressure drop across the length of a tube bundle, a simple relationship for permeability is obtained as [1],[2]:

$$K_{\text{cond}} = \frac{\varepsilon d^2}{32} \quad (3-6)$$

Noting that $d = d_{\text{void}}$, we can rewrite this as:

$$K_{\text{cond}} = \frac{\varepsilon^3}{2A_0^2} \quad (3-7)$$

Hydraulic Radius – The Carman-Kozeny Model: The Carman-Kozeny [51] theory models a porous medium as consisting of conduits of varying shape but, on an average, a constant cross-sectional area. The permeability, according to this theory, is given by [1]:

$$K_{\text{CK}} = \frac{\varepsilon d^2}{16k_k} \quad (3-8)$$

where k_k is known as the Kozeny constant, and is derived from the average path lengths of flow through the assumed conduit and a ‘shape factor’ associated with it [2]. Noting again, that $d = d_{\text{h,void}}$, we can rewrite this equation as:

$$K_{\text{CK}} = \frac{\varepsilon^3}{k_k A_0^2} \quad (3-9)$$

The Kozeny constant is approximated as 5 for packed beds of spheres; various models describing its dependence on porosity and specific surface have been developed. Some are discussed below.

Happel and Brenner – Flow over cylinders: Happel and Brenner [52] derived solutions to Navier-Stokes equations for flow along the length of assemblies of cylinders. They arrived at the following value of Kozeny constant:

$$k_{\text{K,HB}} = \frac{2\varepsilon^3}{(1-\varepsilon) \left[2 \ln \frac{1}{1-\varepsilon} - 3 + 4(1-\varepsilon) - (1-\varepsilon)^2 \right]} \quad (3-10)$$

Kyan Fibrous Bed Model: Kyan et al. [53] derived an expression for the Kozeny constant based on a correlation between friction factor and Reynolds number obtained considering viscous losses, form drag and the elasticity of the fibers. The Kozeny constant is given as:

$$k_{K,Ky} = \frac{[62.3N_e^2(1-\varepsilon)+107.4]\varepsilon^3[1+f_d]}{16N_e^6(1-\varepsilon)^4} \quad (3-11)$$

where N_e is the ‘effective pore number’, defined as

$$N_e = \left[\frac{2\pi}{1-\varepsilon} \right]^{1/2} - 2.5 \quad (3-12)$$

and f_d is the friction factor due to fiber deflection, which is equal to zero in the case of rigid material, which is the case here.

Packed bed of particles, Rumpf-Gupte: Rumpf and Gupte proposed an empirical correlation for a packed bed of uniformly random particles [54] over a wide range of porosities. The permeability in their case is given by:

$$K_{RG} = \frac{d_p^2 \varepsilon^{5.5}}{5.6a} \quad (3-13)$$

where a is a constant, approximated as 1.05 for a wider particle size distribution and 1 for a narrower one.

The value of particle diameter, d_p is a volume averaged value of particle diameters across the medium and for nonspherical particles, it is calculated as [1]:

$$d_p = \frac{V(S)}{A(I)} = \frac{6(1-\varepsilon)}{A_0} \quad (3-14)$$

Empirical correlations for flow through fibrous beds: Two commonly cited correlations are the following –

Davies equation: Davies proposed an empirical correlation for permeability in flow through fibrous beds [2] from a friction factor formulation:

$$K_{\text{Dav}} = \frac{d_f^2}{64(1-\varepsilon)^{3/2}[1+56(1-\varepsilon)^3]} \quad (3-15)$$

Chen correlation: Another expression for flow through fibrous beds was derived by Chen [55]:

$$K_{\text{Ch}} = \frac{\pi d_f^2 \ln[k_5 / (1-\varepsilon)^{1/2}]}{4k_4} \left(\frac{\varepsilon}{1-\varepsilon} \right) \quad (3-16)$$

with $k_4 = 6.1$, $k_5 = 0.64$.

Brinkman drag model: Brinkman [56] developed an expression for permeability by modeling viscous forces on spherical particles embedded in a porous mass. The permeability is given by:

$$K_{\text{Br}} = \frac{d_p^2}{72} \left(3 + \frac{4}{1-\varepsilon} - 3 \left(\frac{8}{1-\varepsilon} - 3 \right)^{1/2} \right) \quad (3-17)$$

With d_p given by Eq. 3-14, we can rewrite this as:

$$K_{\text{Br}} = \frac{(1-\varepsilon)^2}{2A_0^2} \left(3 + \frac{4}{1-\varepsilon} - 3 \left(\frac{8}{1-\varepsilon} - 3 \right)^{1/2} \right) \quad (3-18)$$

It has been pointed out [2] that this equation yields $K = 0$ for $\varepsilon = 1/3$. However, this model provides good permeability estimates for higher porosities.

2-point correlation bound (Berryman-Milton): From a rigorous formulation of the variational principle for viscous flow through porous media, Berryman and Milton [57] proposed a permeability bound given by:

$$K_{s_2} \leq \frac{2}{3} \int_0^\infty \frac{r(s_2(r) - \varepsilon^2)}{(1 - \varepsilon)^2} dr \quad (3-19)$$

where $s_2(r)$ is the 2-point correlation function of the medium [17]. The two-point correlation, if approximated by two straight lines, given below:

$$\begin{aligned} s_{2,a}(r) &= \varepsilon - \frac{A_0 r}{4} ; 0 < r < \frac{4\varepsilon(1 - \varepsilon)}{A_0} \\ s_{2,a}(r) &= \varepsilon^2 ; \frac{4\varepsilon(1 - \varepsilon)}{A_0} \geq r \end{aligned} \quad (3-20)$$

yields, upon integration,

$$K_{s_{2,a}} \approx \frac{16}{9} \frac{\varepsilon^2}{A_0^2} (1 - \varepsilon) \quad (3-21)$$

3.2.2.2 Models for Dupuit-Forchheimer coefficient (non-Darcy coefficient):

Relations predicting the Dupuit-Forchheimer coefficient (non-Darcy coefficient) are often proportional to the inverse of the square root of the medium permeability. Some models consider an explicit dependence of the coefficient on porosity while others have suggested an implicit dependence through the inclusion of higher indices of inverse permeability. The commonly used models are given below.

Ergun equation and the Modified-Ergun (Macdonald et. al's) equation: Ergun [58], calculated the pressure drop and friction factor for arrangements of granular columns. From his

friction factor equations, the following correlation for the Forchheimer coefficient can be arrived at:

$$F_E = \frac{1.75}{\sqrt{150\varepsilon^3}} \frac{1}{\sqrt{K}} \quad (3-22)$$

Macdonald et al. [59] tested the Ergun equation for friction factor of a bed of particles f_p [60] to arrive at the following relations for Forchheimer coefficient, for a packed bed of smooth particles:

$$F_M = \frac{1.8}{\sqrt{180\varepsilon^3}} \frac{1}{\sqrt{K}} \quad (3-23)$$

Ward's correlation: Ward [61] suggested an implicit dependence on porosity through dimensional analysis and proposed the following correlation:

$$F_W = \frac{0.55}{\sqrt{K}} \quad (3-24)$$

Geertsma's relation: Geertsma [62] studied various consolidated and unconsolidated media and arrived at a relation combining the effect of porosity and permeability on the Dupuit-Forchheimer coefficient:

$$F_G = \frac{0.005}{\varepsilon^{5.5} K^{1/2}} \quad (3-25)$$

3.3 Methodology

Five samples are selected for the RPC and CaCO₃ packed bed respectively. The porosity and specific surface areas for the samples are given in Table 3-1. The samples in both cases cover a wide range of porosities, allowing for both conduit-flow and drag-flow effects to come into consideration.

Table 3-1. Porosities and specific surface areas of the samples employed

Material	Sample number	Porosity, ε (-)	Specific surface area A_0 (10^3 m^{-1})
RPC	R1	0.727	0.929
	R2	0.792	0.858
	R3	0.863	0.738
	R4	0.913	0.636
	R5	0.954	0.459
CaCO ₃ particle packed bed	C1	0.329	1.38
	C2	0.457	1.45
	C3	0.604	1.25
	C4	0.712	1.03
	C5	0.824	0.763

3.3.1 Mesh Generation and Flow Simulation

Unstructured tetrahedral, body-fitted grids are generated for each of the samples using an in house grid generator making use of the pore-space indicator function [13]. The mesh generator initially tessellates the entire sample volume using identical tetrahedral elements. Then, by placing additional nodes at the solid-void interfacial surfaces, it separates the subvolume to be discretized – in this case, the pore-space – from the remaining volume. The mesh is then refined in the regions close to the solid-void interface, using algorithms described in [63]. Finally, by projecting nodes from interface crossing edges onto the interface i.e. *vertex rounding* and by *cutting* interface crossing elements into smaller elements, the desired degree of refinement is achieved. This mesh generator has been previously successfully used in [50] and [64]. A paper describing the algorithms used in the mesh generator in detail is currently under review [65].

In the present work, surface adaptive grid refinement is used, i.e., the size of a tetrahedral element, defined as the height of the tetrahedron, is directly proportional to its distance from the

solid-void interface. This kind of meshing allows high resolutions at the interface, where large pressure and velocity gradients occur. Away from the interface, the cell size rapidly increases to a preset maximum size.

Stationary, incompressible continuity and momentum equations are solved in the pore space for Reynolds numbers ranging from 0.1 to 200, using ANSYS-CFX. Since the flow is laminar, no turbulence model is necessary. The domain for the solution consists of the porous medium sample embedded in a square channel. A uniform velocity boundary condition is imposed at the inlet and a zero relative pressure condition is imposed at the outlet. The channel walls are assigned a free-slip boundary condition, to simulate isotropy of the porous medium. The solid surfaces within the porous medium feature a no-slip boundary condition.

Figure 3-1 shows a schematic of the computational domain. Figure 3-2 shows sectional views of domain mesh samples for the RPC and the CaCO_3 particle packed bed.

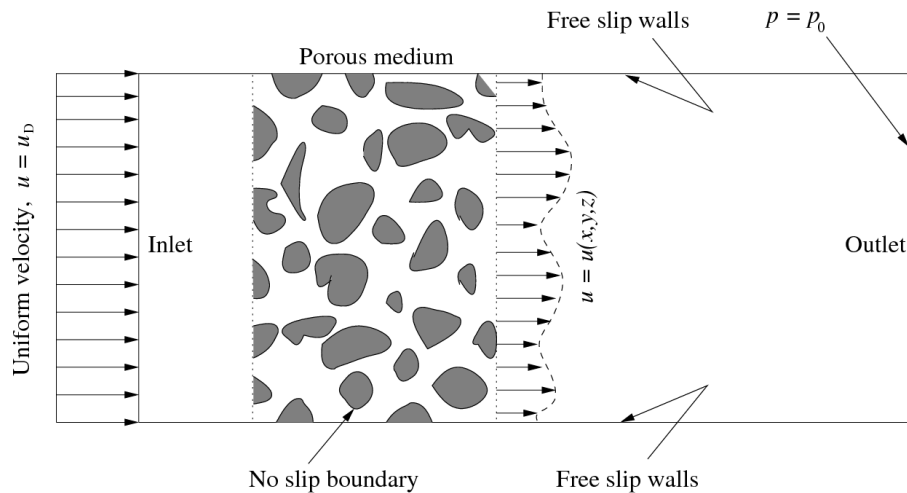


Figure 3-1. Computational domain and boundary conditions.

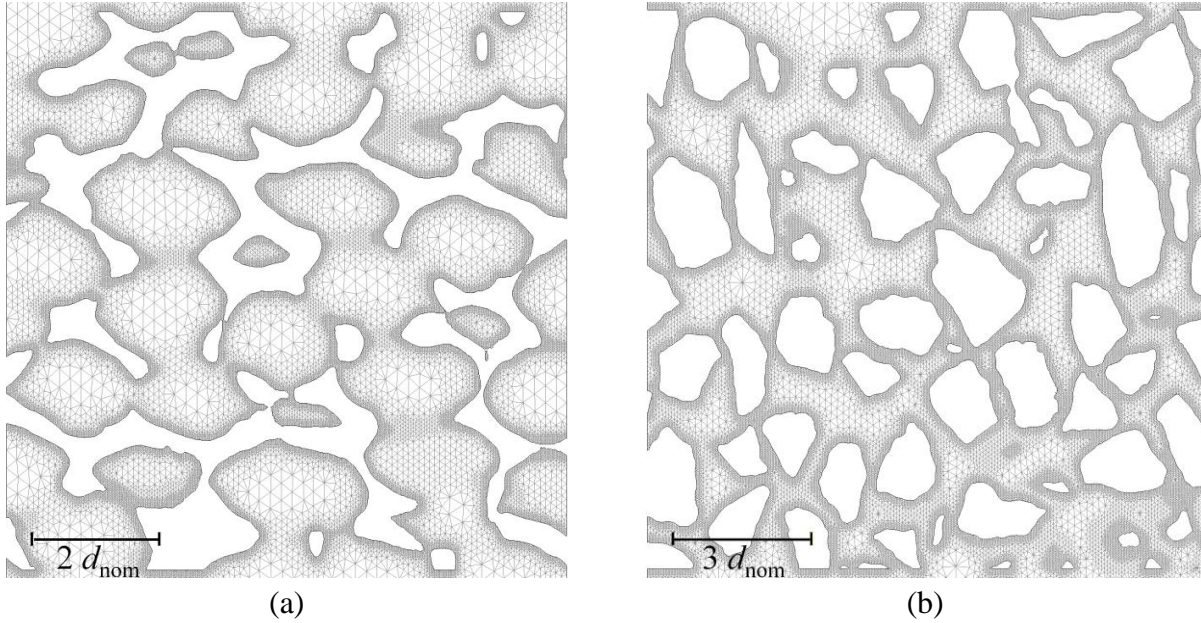


Figure 3-2. Sectional views of tetrahedral grids generated in pore-space of (a) RPC sample R1 and (b) CaCO_3 particle bed sample C3. It can be seen that the grid is very fine and dense at the solid-void interface and element sizes rapidly converge to the preset maximum.

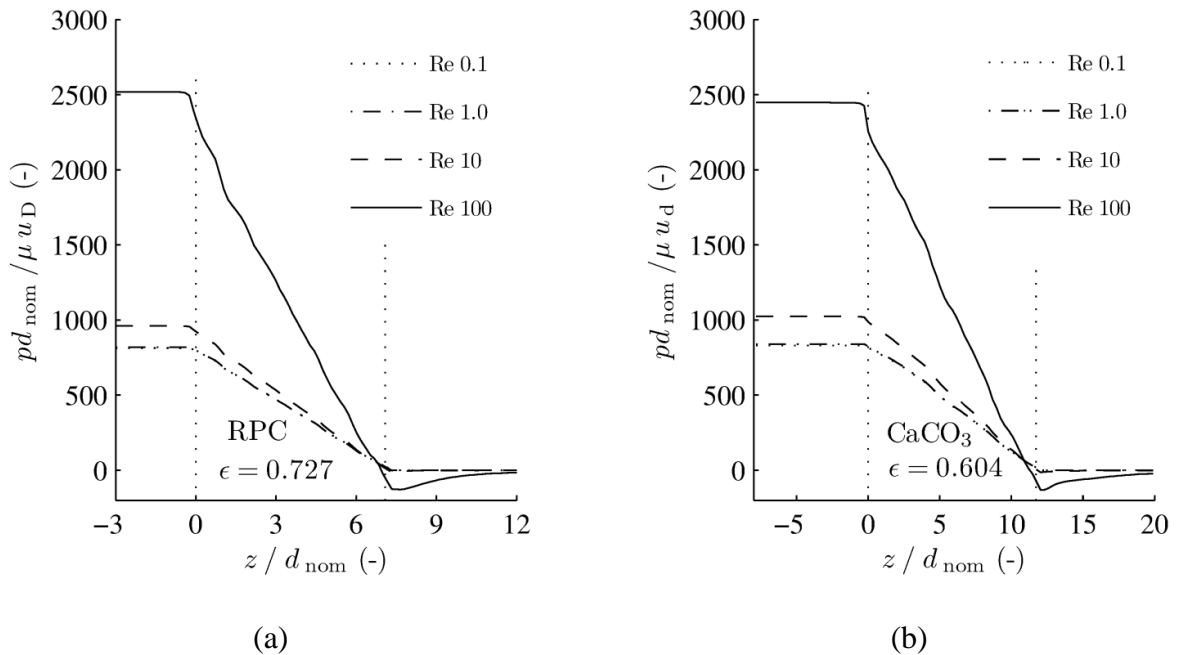


Figure 3-3. Dimensionless pressure along the length of a sample for increasing Reynolds numbers: (a) RPC sample R3 and (b) CaCO_3 particle packed bed sample C3.

In each case, the cross-sectional mean pressure profile in the fluid phase is obtained and subsequently used to determine the mean pressure gradient across the sample. From the dimensionless pressure gradients, the inverse dimensionless permeability and the dimensionless Dupuit-Forchheimer coefficient are calculated. Sample pressure profiles through the media are shown in Figure 3-3. For Re 0.1-1.0, the profiles overlap as the pressure drop is governed by permeability alone, at higher Re, the Dupuit-Forchheimer term starts to become distinct, and dimensionless pressure drop increases.

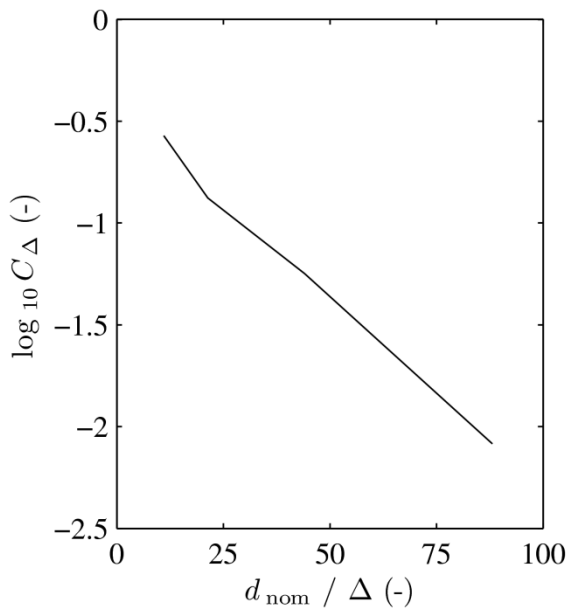
3.3.2 Representative Mesh and Sample Length Scales

Grid refinement and sample size are determined through convergence studies. For both the RPC and the CaCO₃ packed bed samples, grid refinement was studied on a sample of size 128 × 128 × 128 voxels. For the RPC, grids with representative mesh length scales ranging from 14.4 μm to 231 μm were studied for a sample of porosity 0.73. For the CaCO₃ packed bed, the representative length scales ranged from 33.8 μm to 90 μm, for a sample of porosity 0.60. The pressure drop across the sample for each level is calculated for flow at Re=200 and the relative convergence of pressure drop, defined as:

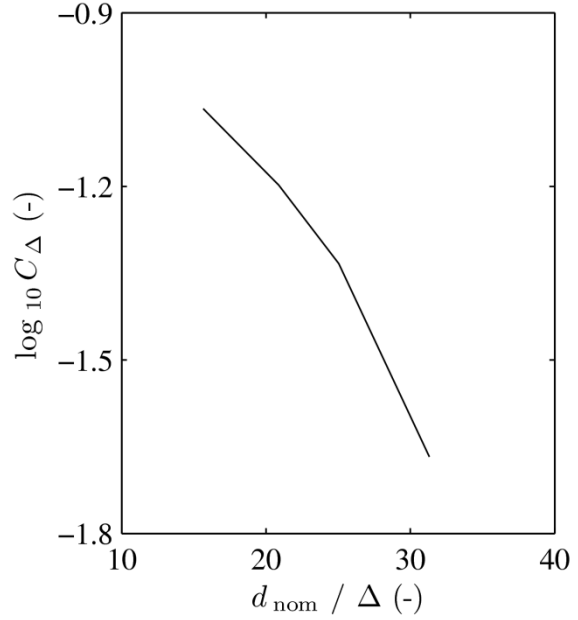
$$C_{\Delta} = \frac{\|\Delta p_1 - \Delta p_{\text{ref}}\|}{\Delta p_{\text{ref}}}$$

(3-26)

where Δp_{ref} is the pressure drop across the sample with the finest grid. The relative convergence is plotted against the ratio of sample nominal diameter to mesh representative length scale, A , in Figure 3-4.



(a)



(b)

Figure 3-4. Pressure drop convergence vs. grid refinement for (a) RPC sample R1 and (b) CaCO_3 particle packed bed sample C3.

Based on the results of the grid convergence, a mesh length scale of $45 \mu\text{m}$, corresponding to $0.018d_{\text{nom}}$ was selected for the RPC. The mesh length scale for CaCO_3 also was also found to be $45 \mu\text{m}$, or $0.022d_{\text{nom}}$.

In order to determine a representative but not overly large sample cube sample convergence studies were carried out. RPC sample cubes ranging from $128 \times 128 \times 128$ voxels to $640 \times 640 \times 640$ voxels from sample R1, were studied in $\text{Re}=200$ flow simulations. For the CaCO_3 bed, samples ranging from $64 \times 64 \times 64$ voxels to $384 \times 384 \times 384$ voxels were studied.

Convergence of the pressure drop per unit length of the sample is examined:

$$C_v = \frac{\|(\Delta p_i / L_i) - (\Delta p_{\text{ref}} / L_{\text{ref}})\|}{(\Delta p_{\text{ref}} / L_{\text{ref}})} \quad (3-27)$$

where $(\Delta p_{\text{ref}}/L_{\text{ref}})$ is the pressure drop per unit length across the largest sample in each case. The convergence plots are shown in figure 3-5.

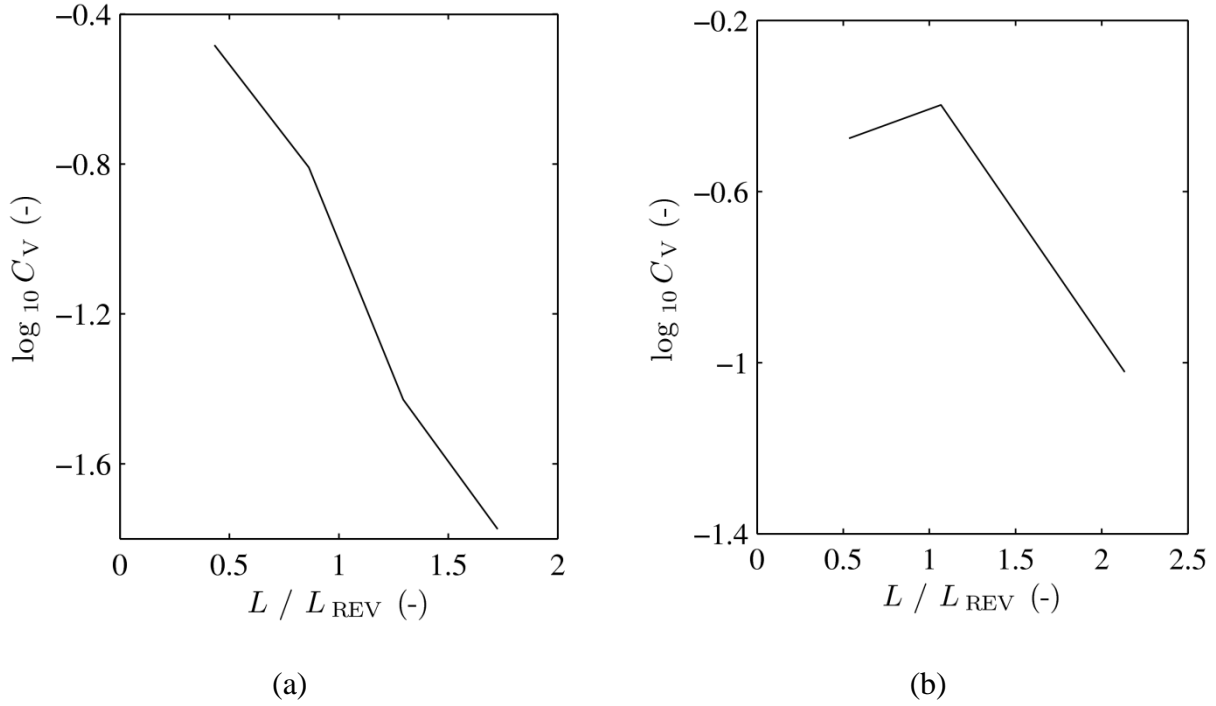


Figure 3-5. Convergence of pressure drop per unit length vs. sample size for (a) RPC sample R1 and (b) CaCO_3 particle packed bed sample C3.

In the determination of permeability and Dupuit-Forchheimer coefficient, for the RPC samples, a cube of edge length 640 voxels, corresponding to $L/L_{\text{REV}} = 2.2$ was selected. For the CaCO_3 particle bed samples, the cube used was of edge length 384 voxels, i.e. $L/L_{\text{REV}} = 3.2$. This resulted in meshes with 4.10×10^7 tetrahedrals for the sample with the lowest specific surface, A_0 and 7.07×10^7 tetrahedrals for the sample with the highest specific surface, in case of the RPC, and meshes with number of tetrahedrals equal to 4.47×10^7 and 6.80×10^7 respectively for the CaCO_3 samples.

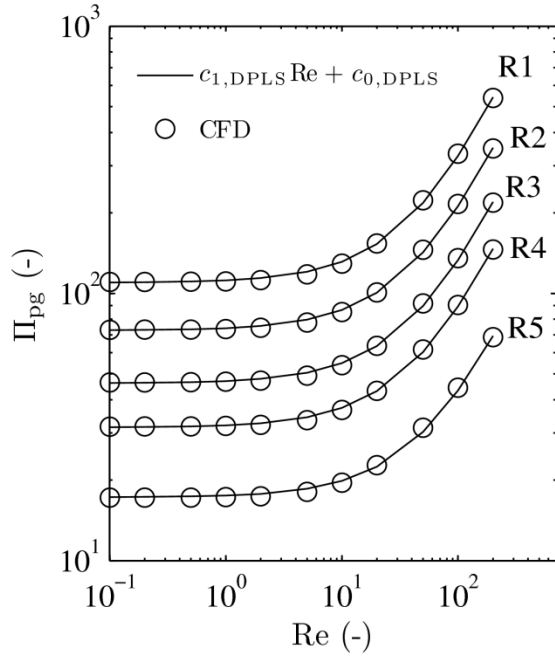
3.4 Results

The DPLS results for permeability and Dupuit-Forchheimer coefficient for the RPC and CaCO₃ are given in table 3-2. Normalized RMS errors (NRMSE) for the straight line fit of pressure drop with Eq. 3-4 have also been tabulated in table 3-2. Figure 3-6 shows the curves for the least squares fit values of c_0 and c_1 and the CFD results for the normalized pressure drop, Π_{pg} for the RPC and CaCO₃ samples. The results for the permeability, K , calculated from the models listed in section 2.2, have been plotted in figure 3-7 below. In general, Dupuit-Forchheimer type equations fit the CFD results well.

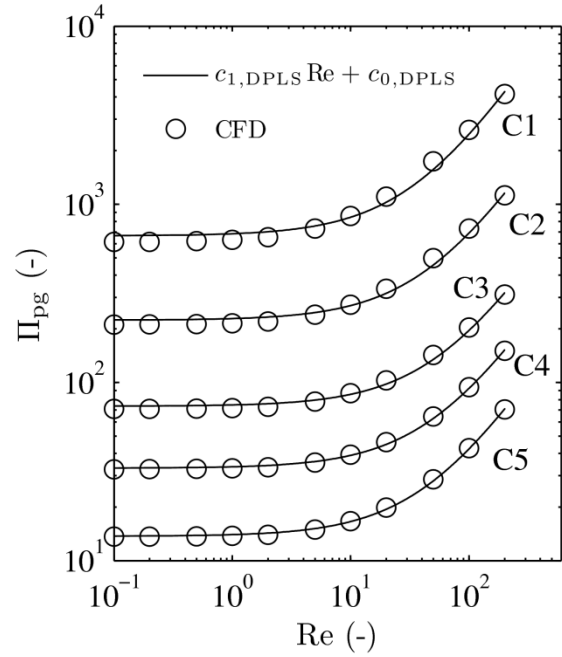
Table 3-2. Permeability and Dupuit-Forchheimer coefficient values for the RPC and CaCO₃ packed bed samples as identified from direct pore level simulation.

Material	Sample	K_{DPLS} (10^{-7} m ²)	c_0 (-)	F_{DPLS} (m ⁻¹)	c_1 (-)	NRMSE (%)
RPC	R1	0.59	110	852	2.16	0.73
	R2	0.89	72.7	548	1.39	0.70
	R3	1.39	46.1	342	0.87	0.69
	R4	2.05	31.5	227	0.58	0.64
	R5	3.74	17.3	102	0.26	1.15
CaCO ₃ particle packed bed	C1	0.03	665	1.28×10^4	18.1	2.47
	C2	0.09	224	3.29×10^3	4.65	2.53
	C3	0.27	73.5	867	1.22	1.91
	C4	0.60	33	422	0.59	0.85
	C5	1.45	13.7	203	0.29	0.54

The values for CaCO₃ are similar for comparable porosity to those for RPC. As such, at high porosity, both the RPC and CaCO₃ structures interact with flow in the form of submerged bodies rather than conduit structures. Then, the pressure drop relates to the drag force exerted on the flow by these structures.

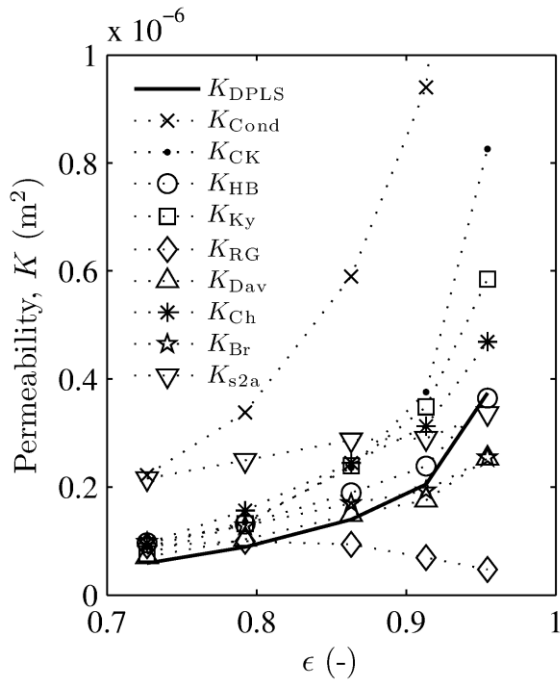


(a)

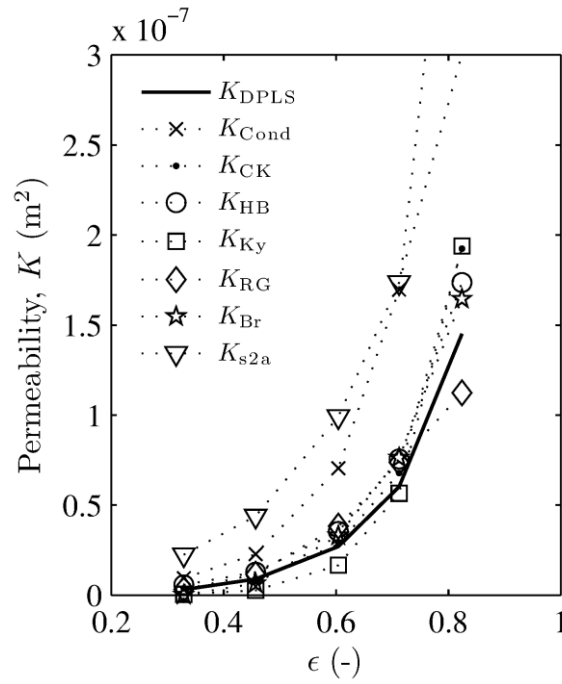


(b)

Figure 3-6. DPLS results and fitting results for normalized pressure drops for (a) RPC samples and (b) CaCO_3 packed bed samples.



(a)



(b)

Figure 3-7. Permeability vs. porosity for (a) RPC samples and (b) CaCO_3 packed bed samples.

The Happel-Brenner [52] relation best predicts the trend of the permeability with porosity for the RPC, while the Brinkman [56] model applies well to the packed bed of CaCO_3 particles, especially at high porosities. With a porosity dependent relationship for the Kozeny constant, the Kyan [53] fibrous bed model also effectively predicts the permeability for the RPC. The empirical Chen [55] and Davies [2] fibrous bed models are reasonably accurate for the RPC whereas the Rumpf-Gupte [54] model performs well within the porosity range considered for the CaCO_3 packed bed. This agrees well with the data given in [1,2]. The s_2 permeability bound approximation [57] results describe very high permeability bounding values.

NRMSE of K from model predictions with respect to K_{DPLS} are shown in table 3-3, for the sample media.

Table 3-3. RMS errors of the results for permeability for different models, across all porosities, for the sample media.

Model	Normalized RMS error (%)	
	RPC	CaCO_3
Conduit Flow	273	121
Carman-Kozeny	70.3	15.1
Happel-Brenner, Parallel Flow	11.8	10.7
Kyan, Fibrous Beds	39.4	15.9
Rumpf-Gupte, Packed Beds	50.9	11.7
Davies, Fibrous Beds	17.9	-
Chen, Fibrous Beds	27.5	-
Brinkman Drag Model	19.3	8.26
2-point Correlation Approximation	40.4	65.9

The Kozeny constant for each of the media is corrected using a least-squares fit to the permeability data. The corrected Kozeny constant for the RPC is found to be equal to 7.73, with a NRMS error of 4.16% and that of the CaCO_3 sample is evaluated at 6.10, with a NRMS error of 3.37%. The plots for the Carman-Kozeny relationship with the corrected constants are given in figure 3-8.

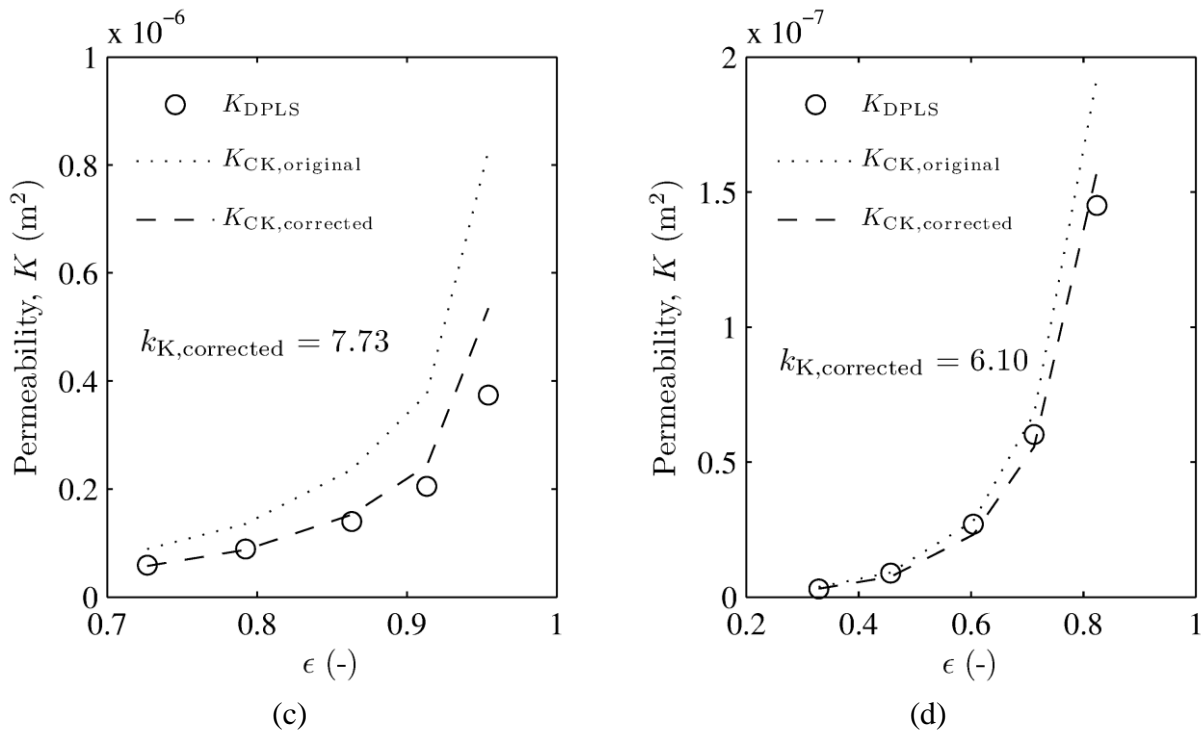


Figure 3-8. Permeability vs. porosity for (a) RPC and (b) CaCO_3 packed bed for corrected Kozeny constants. Also plotted are the DPLS results.

The Dupuit-Forchheimer coefficient is plotted for both media using the correlations described in equations 3-22 to 3-25, in figure 3-9 below. Satisfactory fits for this correlation are difficult to find in case of many of the analytical models, especially for the RPC. This is in part due to the fact that the relationships were developed for flow of fluids through much ‘tighter’

media, such as sheet rock, as early developments in this direction were entirely due to water-drainage and petroleum extraction research.

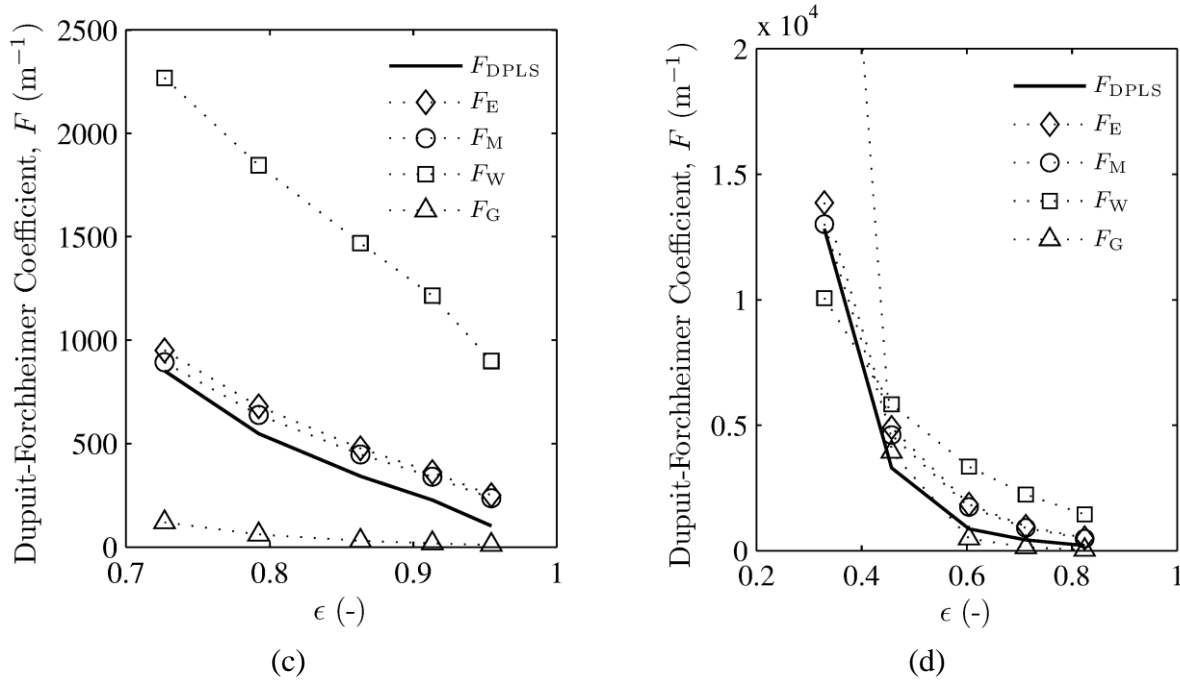


Figure 3-9. Dupuit-Forchheimer coefficient vs. porosity for (a) RPC samples and (b) CaCO₃ samples.

The NRMS errors of the results for the Dupuit-Forchheimer coefficient are given in table 3-4 for both the media.

Table 3-4. RMS errors of the results for predicted Dupuit-Forchheimer coefficient, across all porosities, for the sample media

Model	Normalized RMS error (%)	
	RPC	CaCO ₃
Ergun	17.4	7.93
Modified Ergun (Macdonald)	13.5	5.94
Ward	153	17.7
Geertsma	57.4	101

It is seen that in case of, both, the permeability and the Dupuit-Forchheimer coefficient, hydraulic radius models predict the trend of variation reasonably well, for both sample media. For the RPC, the permeability is well predicted by the implicit inclusion of a drag model through Kyan's fibrous bed model [53]. The behavior of the CaCO₃ packed bed is also predicted with high accuracy by the Rumpf-Gupte [54] model, as described in [2]. The correlations for the Dupuit-Forchheimer coefficient suffer from lack of accuracy in both cases, since the constants used in the generic equation of the form,

$$F = \frac{b}{K^m \varepsilon^n}$$

(3-28)

are empirical [66] and need adjustment per case. Cooke [67] suggested using a correlation independent of the porosity, of the form:

$$F = \frac{b}{K^m}$$

(3-29)

From least squares fitting of the results for the Dupuit-Forchheimer coefficient to equation (29), we get values of $b = 1.41 \times 10^{-5}$ and $m = 1.08$ for the RPC sample, with NRMSE of fitted coefficients 0.96% and $b = 4.06 \times 10^{-7}$ and $m = 1.23$ for the CaCO₃ packed bed, with NRMSE of fit equal to 0.53%. Cooke [67] suggested using $m = 1.24$ for particle packs with particle sizes ranging from 1.68 mm – 2.38 mm (mesh sizes 8-12). Conversely, Thauvin and Mohanty [68] used a network model to suggest that in a porosity-independent relation for the Dupuit-Forchheimer coefficient, $m = 1$. Using $m = 1$ in equation (29), we get $b = 4.92 \times 10^{-5}$ m for the RPC with an NRMSE of 2.22% and $b = 3.72 \times 10^{-5}$ m for the CaCO₃ packed bed with an NRMSE of 3.92%, while Thauvin and Mohanty predict a value of 2.47×10^{-5} . Nevertheless, the

inverse of the permeability is seen to reasonably predict the behavior of the Dupuit-Forchheimer coefficient with porosity variation.

3.5 Summary

Direct numerical simulation of incompressible, stationary flow in reticulate porous ceramics and packed beds of CaCO_3 has been carried out based on tomographic data that has been modified using image processing techniques to obtain a wide range of porosities. Unstructured finite-volume grids have been generated for porous media samples based on the modified tomography data. Flow in the Reynolds number range from 0.1 to 200 has been simulated. From the Dupuit-Forchheimer equation (i.e., the modified Darcy equation) and using the numerical results for pressure gradient, the medium permeability and Dupuit-Forchheimer coefficient have been determined. Various empirical and geometrical models for permeability and Dupuit-Forchheimer coefficient have been compared to the numerical results.

It has been shown that the Happel-Brenner (parallel flow over cylinders) model predicts the permeability of the RPC samples within an NRMSE of 11.8% and the Brinkman model predicts the permeability of the packed bed within 8.26%. The Brinkman model, however, is not applicable at low porosities, approaching a permeability of zero at $\varepsilon = 1/3$. The Kyan model with a porosity dependent Kozeny constant and the Rumpf-Gupte model for packed beds predict the permeability of both materials satisfyingly over a wide range of porosities. Adjustment of the Kozeny constant extends the applicable range of porosity. The adjusted Kozeny constant of the RPCs has been determined as 7.73 and the Kozeny constant of packed beds of CaCO_3 has been determined as 6.10. In case of both, the RPC and the CaCO_3 packed bed, the Modified Ergun (Macdonald et al.) model shows the least normalized RMS error, of 13.5% and 5.94%, respectively, in predicting the Dupuit-Forchheimer coefficient. The Geertsma correlation

produces valid results at high porosities for the CaCO_3 particle packed bed sample, but not for the RPC sample. The Ward correlation fails to predict the Dupuit-Forchheimer coefficient with adequate accuracy in case of both materials.

In conclusion, all permeability and Dupuit-Forchheimer models investigated show at least some degree of deviation from direct pore-level numerical simulation. The techniques described in this paper can be used to accurately characterize the flow parameters of a porous medium without the need for expensive experimentation. The reliance on models, with their inherent underlying assumptions, can thus be reduced. At the same time, for materials with similar morphological characteristics, this technique can be used to develop models for fluid flow specific to that class of materials.

CHAPTER 4 SCOPE AND OUTLOOK

4.1 Accomplishments

The unique transport properties of macroporous media, arising from their complex geometrical characteristics, offer scope for novel engineering applications of these media [3]. A model-based approach typically used for continuum analysis and design of such applications relies heavily on the accurate determination of effective transport properties. Tomography-based numerical simulation of transport phenomena [13] has been shown to be a plausible means of approaching this problem. Manipulation of tomography data through image processing techniques adds the capability of parameter-based analysis of thermal properties [47]. This has been shown in case of radiative heat transfer (chapter 2) and Darcian fluid flow (chapter 3) through such media.

4.2 Future Scope

4.2.1 Solid Phase Conduction and Combined Conduction, Convection and Radiation Modeling

The analysis of multi-scale conduction heat transfer in fluid-saturated RPCs using tomography based methods has been demonstrated in [69]. Using similar methods and by applying the manipulations to tomography data as in earlier chapters, porosity-dependent relationships for the effective thermal conductivity of the porous media can be obtained. The solution can further be extended to cover combined conductive, convective and radiative heat transfer within the media. This will be useful in addressing, for example, reactive flows occurring in processes such as catalytic conversion, hydrogen generation etc. more rigorously.

4.2.2 Multi-objective Optimization and Transient Process Simulation

Multi-objective optimization to determine the ideal pore-structure and porosity of a medium sample to be used in a process involving all three modes of heat transfer, e.g. solar thermochemical hydrogen production [8] can be a further extension of the capabilities of tomography data based modeling. While an engineered porous structure predicted through such optimization may not be readily manufacturable, naturally occurring or synthetic porous media with morphology closely approaching the optimized medium may be selected to achieve higher process efficiency.

Transient modeling of heat transfer within the porous medium space, e.g. [7] is another key area of interest in thermochemical processes. In most cases, analytical models for porous media, such as packed beds of spheres, are employed to cover their geometrical character. While this may be computationally expensive, erosions and dilations dependent on reaction kinetics can be included in a combined simulation of heat transfer processes to closely mimic the actual system. The results can be used to guide process parameter settings.

4.3 Tailored Media

Within a limit, porous ceramics can be manufactured at a preset porosity by adjusting ceramic slurry viscosity [12]. Similar manipulation can be effected, by controlling particle sizes and/or fluidization parameters, for packed beds [36]. Graded porosity media can also be obtained by combined adjustments to the manufacturing process. In order to achieve the optimum medium configuration as suggested by tomography-based numerical simulations, the manufacturing process can be adapted to include some of such tailoring. This opens another avenue of process efficiency improvement for the outlined cases.

LIST OF REFERENCES

- [1] M. Kaviany, Principles of Heat Transfer in Porous Media, 2nd ed., Springer, 1995.
- [2] F. Dullien, Porous media: fluid transport and pore structure, Academic Press Inc, New York, 1979.
- [3] I. Nettleship, Applications of Porous Ceramics, Key Engineering Materials. 122-124 (1996) 305–324.
- [4] S.B. Sathe, R.E. Peck, T.W. Tong, A numerical analysis of heat transfer and combustion in porous radiant burners, International Journal of Heat and Mass Transfer. 33 (1990) 1331–1338.
- [5] C.-J. Tseng, J.R. Howell, Combustion of Liquid Fuels in a Porous Radiant Burner, Combustion Sc. & Tech. 112 (1996) 141–161.
- [6] A.L. Dicks, Hydrogen generation from natural gas for the fuel cell systems of tomorrow, Journal of Power Sources. 61 113–124.
- [7] W. Lipinski, A. Steinfeld, Transient radiative heat transfer within a suspension of coal particles undergoing steam gasification, Heat Mass Transfer. 41 (2005) 1021–1032.
- [8] A. Steinfeld, Solar thermochemical production of hydrogen--a review, Solar Energy. 78 (2005) 603–615.
- [9] A. Cybulski, Structured catalysts and reactors, 2nd ed., Taylor & Francis, Boca Raton, 2006.
- [10] J. Adler, Ceramic Diesel Particulate Filters, International Journal of Applied Ceramic Technology. 2 (2005) 429–439.
- [11] S. Whitaker, The method of volume averaging, Kluwer Academic, Dordrecht; Boston, 1999.
- [12] A.R. Studart, U.T. Gonzenbach, E. Tervoort, L.J. Gauckler, Processing Routes to Macroporous Ceramics: A Review, J American Ceramic Society. 89 (2006) 1771–1789.
- [13] J. Petrasch, Tomography-based Methods for Reactive Flows in Porous Media, VDM Verlag, 2009.
- [14] R.C. Gonzalez, Digital Image Processing, 2nd ed., Prentice Hall, 2002.
- [15] J. Petrasch, P. Wyss, A. Steinfeld, Tomography-based Monte Carlo determination of radiative properties of reticulate porous ceramics, Journal of Quantitative Spectroscopy and Radiative Transfer. 105 (2007) 180–197.

- [16] S. Haussener, W. Lipinski, J. Petrasch, P. Wyss, A. Steinfeld, Tomographic Characterization of a Semitransparent-Particle Packed Bed and Determination of its Thermal Radiative Properties, *J. Heat Transfer*. 131 (2009) 072701–11.
- [17] J. Petrasch, P. Wyss, R. Stämpfli, A. Steinfeld, Tomography-Based Multiscale Analyses of the 3D Geometrical Morphology of Reticulated Porous Ceramics, *Journal of the American Ceramic Society*. 91 (2008) 2659–2665.
- [18] J.R. Howell, M.J. Hall, J.L. Ellzey, Combustion of hydrocarbon fuels within porous inert media, *Progress in Energy and Combustion Science*. 22 (1996) 121–145.
- [19] V.R. Choudhary, B.S. Uphade, A.S. Mamman, Oxidative Conversion of Methane to Syngas over Nickel Supported on Commercial Low Surface Area Porous Catalyst Carriers Precoated with Alkaline and Rare Earth Oxides, *Journal of Catalysis*. 172 (1997) 281–293.
- [20] T. Fend, B. Hoffschmidt, R. Pitz-Paal, O. Reutter, P. Rietbrock, Porous materials as open volumetric solar receivers: Experimental determination of thermophysical and heat transfer properties, *Energy*. 29 823–833.
- [21] D. Baillis, J.-F. Sacadura, Thermal radiation properties of dispersed media: theoretical prediction and experimental characterization, *Journal of Quantitative Spectroscopy and Radiative Transfer*. 67 (2000) 327–363.
- [22] T. Osinga, W. Lipinski, E. Guillot, G. Olalde, A. Steinfeld, Experimental Determination of the Extinction Coefficient for a Packed-Bed Particulate Medium, *Experimental Heat Transfer*. 19 (2006) 69–79.
- [23] M.B. MJ Hale, Measurement of the radiative transport properties of reticulated alumina foams, in: Washington, DC (United States), 1992.
- [24] B. Rousseau, L. del Campo, J.-Y. Rolland, D. de Sousa Meneses, P. Echegut, Modelling of the Thermal Radiative Properties of Oxide Ceramics, in: 2010 14th International Heat Transfer Conference, Volume 5, Washington, DC, USA, 2010: pp. 933–938.
- [25] B.P. Singh, M. Kaviany, Modelling radiative heat transfer in packed beds, *International Journal of Heat and Mass Transfer*. 35 (1992) 1397–1405.
- [26] B.P. Singh, M. Kaviany, Independent theory versus direct simulation of radiation heat transfer in packed beds, *International Journal of Heat and Mass Transfer*. 34 (1991) 2869–2882.
- [27] M. Tancrez, J. Taine, Direct identification of absorption and scattering coefficients and phase function of a porous medium by a Monte Carlo technique, *International Journal of Heat and Mass Transfer*. 47 (2004) 373–383.

- [28] J. Randrianalisoa, D. Baillis, Radiative properties of densely packed spheres in semitransparent media: A new geometric optics approach, *Journal of Quantitative Spectroscopy and Radiative Transfer*. 111 (2010) 1372–1388.
- [29] B. Zeghondy, E. Iacona, J. Taine, Determination of the anisotropic radiative properties of a porous material by radiative distribution function identification (RDFI), *International Journal of Heat and Mass Transfer*. 49 (2006) 2810–2819.
- [30] C. Argento, D. Bouvard, A ray tracing method for evaluating the radiative heat transfer in porous media, *International Journal of Heat and Mass Transfer*. 39 (1996) 3175–3180.
- [31] R. Siegel, J. Howell, *Thermal Radiation Heat Transfer*, 2nd ed., McGraw Hill, 1981.
- [32] M.F. Modest, *Radiative Heat Transfer*, 2nd ed., Academic Press, 2001.
- [33] E. Nisipeanu, P.D. Jones, Comparison of Monte Carlo Surface Exchange With Radiative Continuum Results in Large Particle Dispersions, *J. Heat Transfer*. 122 (2000) 503–508.
- [34] J. Petrasch, S. Haussener, W. Lipinski, Discrete vs. continuum scale simulation of radiative transfer in semitransparent two-phase media, in: Antalya, Turkey, 2010.
- [35] T. Tong, S. Sathe, R. Peck, Improving the performance of porous radiant burners through use of sub-micron size fibers, *International Journal of Heat and Mass Transfer*. 33 (1990) 1339–1346.
- [36] G.E. Imoberdorf, F. Taghipour, M. Keshmiri, M. Mohseni, Predictive radiation field modeling for fluidized bed photocatalytic reactors, *Chemical Engineering Science*. 63 (2008) 4228–4238.
- [37] J.T. Farmer, J.R. Howell, Comparison of Monte Carlo Strategies for Radiative Transfer in Participating Media, in: *Advances in Heat Transfer*, Elsevier, 1998: pp. 333–429.
- [38] C. Sagan, J.B. Pollack, Anisotropic Nonconservative Scattering and the Clouds of Venus, *Journal of Geophysical Research*. 72 (1967) 469–477.
- [39] P. Hsu, J.R. Howell, Measurements of thermal conductivity and optical properties of porous Partially Stabilized Zirconia, *Experimental Heat Transfer*. 5 (1992) 293 – 313.
- [40] T.J. Hendricks, J.R. Howell, Absorption/Scattering Coefficients and Scattering Phase Functions in Reticulated Porous Ceramics, *J. Heat Transfer*. 118 (1996) 79–87.
- [41] R. Hilfer, Transport and Relaxation Phenomena in Porous Media, in: I. Prigogine, S.A. Rice (Eds.), *Advances in Chemical Physics*, John Wiley & Sons, Inc., Hoboken, NJ, USA, n.d. pp. 299–424.

- [42] F.M. Auzerais, J. Dunsmuir, B.B. Ferréol, N. Martys, J. Olson, T.S. Ramakrishnan, et al., Transport in sandstone: A study based on three dimensional microtomography, *Geophysical Research Letters*. 23 (1996) 705.
- [43] B. Ferrol, D.H. Rothman, Lattice-Boltzmann simulations of flow through Fontainebleau sandstone, *Transport in Porous Media*. 20 (1995) 3–20.
- [44] H.-J. Vogel, K. Roth, Quantitative morphology and network representation of soil pore structure, *Advances in Water Resources*. 24 233–242.
- [45] M. Rintoul, S. Torquato, C. Yeong, D. Keane, S. Erramilli, Y. Jun, et al., Structure and transport properties of a porous magnetic gel via x-ray microtomography, *Physical Review E*. 54 (1996) 2663–2669.
- [46] S. Haussener, Tomography-based determination of effective heat and mass transport properties of complex multi-phase media, ETH, 2010.
- [47] A. Akolkar, J. Petrasch, Tomography based pore-level optimization of radiative transfer in porous media, *International Journal of Heat and Mass Transfer*. 54 (2011) 4775–4783.
- [48] J. Dupuit, Études théoriques et pratiques sur le mouvement des eaux dans les canaux découverts et à travers les terrains perméables: avec des considérations relatives au régime des grandes eaux, au débouché à leur donner, et à la marche des alluvions dans les rivières à fond mobile, Dunod, 1863.
- [49] P. Forchheimer, Wasserbewegung durch Boden, *Z. Ver. Deutsch. Ing.* 45 (1901) 1782–1788.
- [50] J. Petrasch, F. Meier, H. Friess, A. Steinfeld, Tomography based determination of permeability, Dupuit–Forchheimer coefficient, and interfacial heat transfer coefficient in reticulate porous ceramics, *International Journal of Heat and Fluid Flow*. 29 (2008) 315–326.
- [51] P.C. Carman, Flow of gases through porous media, Butterworths Scientific Publications, 1956.
- [52] J. Happel, Low Reynolds Number Hydrodynamics., Second revised ed., Noordhoff International Publishing, [S.l.], 1973.
- [53] C.P. Kyan, D.T. Wasan, R.C. Kintner, Flow of Single-Phase Fluids through Fibrous Beds, *Ind. Eng. Chem. Fund.* 9 (1970) 596–603.
- [54] H.C.H. Rumpf, A.R. Gupte, Einflüsse der Porosität und Korngrößenverteilung im Widerstandsgesetz der Porenströmung, *Chemie Ingenieur Technik*. 43 (1971) 367–375.

- [55] C.Y. Chen, Filtration of Aerosols By Fibrous Media, *Chemical Reviews*. 55 (1955) 595–623.
- [56] H.C. Brinkman, A calculation of the viscous force exerted by a flowing fluid on a dense swarm of particles, *Applied Scientific Research*. 1 (1949) 27–34.
- [57] J.G. Berryman, G.W. Milton, Normalization constraint for variational bounds on fluid permeability, *The Journal of Chemical Physics*. 83 (1985) 754.
- [58] S. Ergun, Fluid flow through packed columns, *Chemical Engineering Progress*. 48 (n.d.) - 94.
- [59] I.F. Macdonald, M.S. El-Sayed, K. Mow, F.A.L. Dullien, Flow through Porous Media-the Ergun Equation Revisited, *Ind. Eng. Chem. Fund.* 18 (1979) 199–208.
- [60] S. Ergun, A.A. Orning, Fluid Flow through Randomly Packed Columns and Fluidized Beds, *Ind. Eng. Chem.* 41 (1949) 1179–1184.
- [61] J.C. Ward, Turbulent flow in porous media, University of Arkansas, Engineering Experiment Station, 1965.
- [62] J. Geertsma, Estimating the Coefficient of Inertial Resistance in Fluid Flow Through Porous Media, *Society of Petroleum Engineers Journal*. 14 (1974).
- [63] J. Bey, Tetrahedral grid refinement, *Computing*. 55 (1995) 355–378.
- [64] S. Haussener, P. Coray, W. Lipinski, P. Wyss, A. Steinfeld, Tomography-Based Heat and Mass Transfer Characterization of Reticulate Porous Ceramics for High-Temperature Processing, *J. Heat Transfer*. 132 (2010) 023305–9.
- [65] H. Friess, S. Haussener, A. Steinfeld, J. Petrasch, Tetrahedral mesh generation based on space indicator functions, *International Journal for Numerical Methods in Engineering*. (submitted February 2012).
- [66] R.D. Evans, F. Civan, Characterization of non-Darcy multiphase flow in petroleum bearing formations, Oklahoma Univ., Norman, OK (USA). School of Petroleum and Geological Engineering, United States, 1990.
- [67] C.E. Cooke, Conductivity of Fracture Proppants in Multiple Layers, *Journal of Petroleum Technology*. 25 (1973).
- [68] F. Thauvin, K.K. Mohanty, Network Modeling of Non-Darcy Flow Through Porous Media, *Transport in Porous Media*. 31 (1998) 19–37.

- [69] J. Petrasch, B. Schrader, P. Wyss, A. Steinfeld, Tomography-Based Determination of the Effective Thermal Conductivity of Fluid-Saturated Reticulate Porous Ceramics, *Journal of Heat Transfer*. 130 (2008) 032602.

BIOGRAPHICAL SKETCH

Anupam's academic and professional career has been characterized by his love for exploration. Although an engineer by choice, he still actively enjoys a number of artistic pursuits while furthering his engineering research. Anupam began his professional career in 2006 as a Maintenance Engineer in the Heavy Engineering Workshops of Larsen and Toubro Limited, an infrastructure multinational based in India. His work-ethic and detail orientation resulted in a quick promotion to the Design and Engineering Centre of the Weapon Systems Division of the same company. Till mid-2008, he performed the dual duties of a design engineer and a manufacturing liaison on a project for a mid-size Destroyer Class vessel of the Indian Navy.

Returning to academia, Anupam enrolled in the graduate program in Mechanical Engineering at the University of Florida. Specializing in solid mechanics and design, he conducted research in finite-element based structural design and fibre-reinforced composites over a two-year period, before graduating in 2010. Towards the completion of his Master's degree, he was accepted as a Ph.D. student at the University, doing research in the Renewable Energy Laboratory, in the Thermal Sciences division of the Mechanical and Aerospace Engineering Department. His research in radiative heat transfer in porous media has since been published in the International Journal of Heat and Mass Transfer. At present, he is engaged in extending his research in porous media in the area of mass transport.

Anupam completed his Bachelor of Mechanical Engineering, First Class, from the University of Pune, India, in 2006. His final year specialization topic was Robotics and Synthesis of Mechanisms. In keeping with his theme of exploration, he completed a final year project in diesel injection valve design at the Automotive Research Association of India. This project was selected for the Forbes Marshall Best Project Award in his college. During his Bachelor's degree program, Anupam dabbled in a number of co-curricular and extra-curricular activities. He is a

lifetime member of the Boat Club Quiz Club of Pune, an organization active in organizing and promoting trivia quizzing events in Pune. As a member of the Social Activities Committee of his college, Anupam organized remedial tutoring for middle-school and high-school children from underprivileged backgrounds in Pune. He was also the Organizing Secretary of the Literary Society of his college.

Anupam is an avid reader, enjoying both classic and popular fiction. He has earned certification in oil and water-colour painting. He is also a self-professed wine and draft beverage connoisseur.